J. Fluid Mech. (2012), *vol.* 694, *pp.* 464–492.
doi:10.1017/jfm.2011.563

Vorticity forces on an impulsively started finite plate

Jian-Jhih Lee[1], Cheng-Ta Hsieh[1], Chien C. Chang[1,2]† and Chin-Chou Chu[1]†

[1] Institute of Applied Mechanics and Taida Institute of Mathematical Sciences, National Taiwan University, Taipei 106, Taiwan, ROC

[2] Division of Mechanics, Research Center for Applied Sciences, Academia Sinica, Taipei 115, Taiwan, ROC

(Received 30 July 2011; revised 4 December 2011; accepted 16 December 2011; first published online 25 January 2012)

In this study, we consider various contributions to the forces on an impulsively started finite plate from the perspective of a diagnostic vorticity force theory. The wing plate has an aspect ratio (AR) between 1 and 3, and is placed at low and high angles of attack ($\alpha \leqslant$ and $>20°$), while the Reynolds number is either 100 or 300. The theory enables us to quantify the contributions to the forces exerted on the plate in terms of all of the fluid elements with non-zero vorticity, such as in the tip vortices (TiVs), leading- and trailing-edge vortices (LEV and TEV) as well on the plate surface. This line of force analysis has been pursued for two-dimensional flow in our previous studies. In contrast to the pressure force analysis (PFA), the vorticity force analysis (VFA) reveals new salient features in its applications to three-dimensional flow by examining sectional force contributions along the spanwise direction. In particular, at a large aspect ratio ($AR = 3$), the force distributions of PFA and VFA show close agreements with each other in the middle sections, while at a lower aspect ratio ($AR = 1$), the force distribution of PFA is substantially larger than that of VFA in most of the sections. The difference is compensated for by the contributions partly by the edge sections and mainly by the vortices in the outer regions. Further investigation is made fruitful by decomposing the vorticity into the spanwise (longitudinal) component (the only one in two-dimensional flow) and the other two orthogonal (transverse) components. The relative importance of the force contributions credited to the transverse components in the entire flow regions as well as in the two outer regions signifies the three-dimensional nature of the flow over a finite plate. The interplay between the LEV and the TiVs at various time stages is shown to play a key role in distinguishing the force contributions for the plate with a smaller aspect ratio and that with a larger aspect ratio. The present VFA provides a better perspective for flow control by relating the forces directly to the various sources of vorticity (or vortex structures) on or near the wing plate.

Key words: aerodynamics, swimming/flying

1. Introduction

Counter-rotating tip vortices are an important aerodynamic feature of wings of finite span due to the pressure difference between the upper and lower wing surfaces.

† Email addresses for correspondence: mechang@iam.ntu.edu.tw, chucc@iam.ntu.edu.tw

Tip vortices (TiVs) can cause undesirable noise and vibrations as well as induce downwash, which increases the drag force on the wing. Scientists and engineers continue to investigate the effects of TiVs and try to address these problems under various flow conditions. In recent years, research in TiVs has shifted into low-Reynolds-number flows for understanding of animal locomotion with applications to development in micro air vehicles (MAVs) and small unmanned aerial vehicles (UAVs). Because the wing geometry of animal wings and fins typically has a low aspect ratio (LAR), the induced flow is unsteady, and the influence of tip flow is obviously significant. As a model problem, impulsively started LAR plates at low Reynolds number can provide an in-depth research topic that is relevant to the design of small aircraft and the aerodynamics of animal locomotion.

A LAR plate with various angles of attack (AoAs) creates strong TiV structures at low-Reynolds-number flows. In the past, a number of studies on LAR have highlighted the importance of TiV effects; however, most of them have considered that at higher Reynolds numbers. Through experimental studies, Winter (1936) reported that a combined vortex system around a LAR wing consists of a bound vortex and a wing-tip flow characterized by two counter-rotating TiVs. This bound vortex generates downwash and sidewash flows distributed along the wing. In general, a downwash has an influence on the linear lift and induces drag. A sidewash results in the formation of a shear layer at two side edges of a wing, generating TiVs. Bartlett & Vidal (1955) conducted experiments and semi-empirical analysis of LAR wings with rectangular and delta planforms of the order of 1 000 000 of Reynolds numbers. However, that study was mainly concerned with the effect of leading- and trailing-edge shapes. Lamar (1976) applied Polhamus's method (Polhamus 1971) to the analysis of non-delta LAR planforms. He noted that the side-edge-suction force, which means that vortices roll up and attach on the upper side of LAR wing, acts in a direction normal to the plate and contributes vortex lift. Recently, more studies on this topic have investigated various approaches because of concerns about low-Reynolds-number bio-fluid mechanics. Torres & Mueller (2004) presented lift, drag and pitching moment characteristics of wings of LAR operating at low Reynolds numbers. They found that as the AoA increased, the location of the centre of lift was shifted toward the trailing edge of the wing. The reason for this shift is related to the nonlinear lift generated by the wing-tip vortices. Cosyn & Vierendeels (2006) performed numerical study of LAR wings with low AoA with a focus on the resulting lift-and-drag force. They validated the numerical results and found appropriate equations for lift and drag with some useful theories on LAR wings originally developed for wings at higher Reynolds numbers (Bollay 1939; Lamar 1974), and produced important experimental results on LAR flat plates at low Reynolds numbers (Torres & Mueller 2004). In addition, they stated that although classical aerodynamic theory can accurately predict the aerodynamics of large-scale aircraft, in particular lift forces, it is generally not applicable for LAR wings in low-Reynolds-number regimes. The reasons are as follows. First, classical aerodynamic theory does not account for complex flow phenomena such as laminar separation bubbles. Such bubbles are difficult to control and have a generally negative drawback on drag. The second reason is the limited research and aerodynamic models that exist on LAR wings. Theories on LAR wings exist, but they are mainly focused on delta planforms for transonic and supersonic airplanes. Ringuette, Milano & Gharib (2007) experimentally investigated drag force generated by the vortex structure of plates of $AR = 6$ or 2 at $\alpha = 90°$, which is akin to the propulsive half-stroke of an insect wing. They found that the TiVs contribute substantially to the plate force, and the interaction between the TiV and leading-edge

vortex (LEV) results in a transient high drag peak. The work by Taira & Colonius (2009) is closely related to the interest of the present study. They carried out numerical simulations of three-dimensional flows over LAR flat plates to explore the behaviours of the flows and the corresponding forces applied on the plate. In particular, they noted that the TiVs could stabilize the flow, while stronger downwash for lower aspect ratio plates might decrease the lift force. Three-dimensional vortex-structure experiments in translating and rotating plates were conducted by Kim & Gharib (2010). They noted that for a LAR plate in translation mode, the tip effects cause a LEV to develop non-uniformly, which finally induces spanwise flow. However, the spanwise flow is not strong enough to suppress the LEVs attached to the plate. More recently, Shyy *et al.* (2010) reviewed recent progress in flapping wings and summarized the mechanism of forces exerted on impulsively started LAR flat plates generated by TiVs at low-Reynolds-number flows with interesting findings: first, TiVs produce a low-pressure area near the wingtip and provide additional lift. Second, TiVs can induce downwash flow, which reduces the effective AoA and consequent lift forces, but increases the drag forces. Third, they can prevent LEVs, which are considered the main lift source, from immediate shedding (an interaction between TiVs and LEV).

In spite of the many important studies on LAR plate aerodynamics, a quantitative analysis that can identify the primary aerodynamic forces and relate them to individual vortex structures is still lacking. In the literature, there are several useful force theories that shed light on different aspects of hydrodynamic or aerodynamic forces. Circulation theory was an early effort toward predicting lift; see, e.g. Howarth (1935) and Sears (1956, 1976). These authors provided insightful relationships between forces and inviscid models in terms of boundary layer separation, vortex shedding and conservation of circulation. Subsequent studies were meant to provide exact means or theories for hydrodynamic forces through a rigourous analysis of the equation for viscous flow; see, e.g. Phillips (1956), Payne (1958), Wu (1981), Quartapelle & Napolitano (1983), and in particular, Kambe (1986), Howe (1995), Wells (1996) and Howe, Lauchle & Wang (2001) for inviscid and viscous flow. On the other hand, Lighthill (1986) developed ideas that validate a separation of hydrodynamic loadings into potential flow forces and vortex-flow forces. The applied force was deliberately explained as the rate of change of a momentum, defined by an absolutely convergent integral. In this study, we investigate the unsteady mechanisms of a LAR plate with different AoA at low-Reynolds-number flows in terms of a diagnostic force representation (Chang 1992; Chang, Yang & Chu 2008). The force representation theory for real viscous flow is used to separate potential forces such as added mass and inertial forces and to distinguish the contributions of individual fluid elements to aerodynamic forces. The theory starts from the D'Alembert theorem that the incompressible potential flow predicts that no force will be exerted on a body if the incident flow is a constant uniform stream. Incompressible potential flow means that there is no single fluid element possessing non-zero vorticity or dilation. It is therefore considered that in a more realistic flow, any fluid element with non-zero vorticity or dilation may be considered a source of the hydrodynamic force. References that are more directly related to the present application for low-Reynolds-number flow can be found in Hsieh, Chang & Chu (2009) and Hsieh *et al.* (2010). In addition, the early idea that forces (drag and lift) experienced by the body in terms of the vorticity distribution (Burgers 1920), which is similar to this present study, was reviewed by Biesheuvel & Hagmeijer (2006). They pointed out the close relationship of Burgers' formula to those of Lighthill (1979, 1986). These authors went further to establish the connection between these earlier formulae and the more recent work on aerodynamic

forces by Kambe (1986) and Howe *et al.* (2001). Finally, we note a recent paper by Magnaudet (2011) which provides a general form for the prediction of loads on a body moving in an arbitrary non-uniform flow.

This article is structured as follows. First, we introduce the auxiliary potential and briefly derive the vorticity force representation in three dimensions. Next, we apply it to examine the effects of the aspect ratio and of the angle of attack for an impulsively started flat plate at low Reynolds numbers. In particular, we compare the differences of the pressure force analysis (PFA) and the vorticity force analysis (VFA), and assess the relative force contributions of individual vorticity components in the entire flow region as well as in the outer regions. The article ends with concluding remarks.

2. Auxiliary potential

A key component in developing the force element representation is to introduce an auxiliary potential. Consider a finite wing (plate) moving in an otherwise quiescent fluid. Let us first determine the nature of the potential solution. The general solution at great distances r from the finite wing in three dimensions is given by

$$\phi = -(\boldsymbol{A}\cdot\boldsymbol{\nabla})\log r + \cdots = -\frac{\boldsymbol{A}\cdot\hat{\boldsymbol{r}}}{r^2} + \cdots \tag{2.1}$$

$$\boldsymbol{\nabla}\phi = -(\boldsymbol{A}\cdot\boldsymbol{\nabla})\boldsymbol{\nabla}\log r + \cdots = -\frac{3(\boldsymbol{A}\cdot\hat{\boldsymbol{r}})\hat{\boldsymbol{r}} - \boldsymbol{A}}{r^3} + \cdots \tag{2.2}$$

where $\hat{\boldsymbol{r}}$ is the unit vector along the direction of $\boldsymbol{r}$. It should be kept in mind that the corresponding velocity $\boldsymbol{\nabla}\phi$ decays like $1/r^3$ in three dimensions. In (2.1), the vector $\boldsymbol{A}$ depends on the actual shape and is independent of the coordinates. The exact $\boldsymbol{A}$ requires a complete solution of the equation $\boldsymbol{\nabla}^2\phi = 0$ (cf. Landau & Lifshitz 1987) and appropriate boundary conditions. In order to analyse various force contributions to the finite wing, the boundary conditions will be specified depending on which force direction is considered. If $\boldsymbol{s}$ is the unit vector along the force direction of interest, then we require $\boldsymbol{n}\cdot\boldsymbol{\nabla}\phi = -\boldsymbol{n}\cdot\boldsymbol{s}$ on the finite wing surface S. Therefore, if the potential function ϕ satisfies its conditions, $\boldsymbol{s}$-direction pressure force applied on the finite wing for real viscous fluid is decomposed to surface vorticity and volume vorticity forces.

3. The vorticity force representation

Consider a uniform flow past a three-dimensional finite wing, as shown in figure 1. The flow caused by the finite wing is assumed to be governed by the Navier–Stokes and incompressibility condition, which are given in dimensionless form,

$$\frac{\partial\boldsymbol{v}}{\partial t} + (\boldsymbol{v}\cdot\boldsymbol{\nabla})\boldsymbol{v} = -\boldsymbol{\nabla}P + \frac{1}{Re}\Delta\boldsymbol{v}; \tag{3.1}$$

$$\boldsymbol{\nabla}\cdot\boldsymbol{v} = 0, \tag{3.2}$$

where $\boldsymbol{v}$ denotes the velocity and P is the pressure, and $Re = \rho Uc/\mu$ is the Reynolds number with ρ the density, μ the viscosity, U the characteristic velocity and c the chord length. The dimensional velocity $\boldsymbol{v}^*$, time t^* and pressure P^* are related to their dimensionless counterparts by $\boldsymbol{v}^* = U\boldsymbol{v}$, $t^* = ct/U$ and $P^* = \rho U^2 P$. Also, the drag and lift coefficients are defined by $C_D = D^*/\rho U^2 A$ and $C_L = L^*/\rho U^2 A$. Here, D^* is the drag, L^* is the lift and A is the planform area (aspect ratio $\times$ c^2). The most

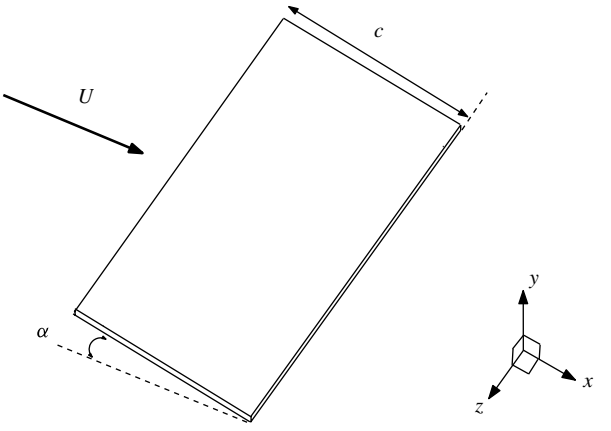

FIGURE 1. Schematic of flow about a plate (finite wing) where U is the inflow velocity in the x-direction, α is the angle of attack (AoA), and c is the chord length.

well-known formula for calculating the drag is

$$C_D = \underbrace{\int_{S_w} P\boldsymbol{n}\cdot\boldsymbol{i}\,\mathrm{d}A}_{C_{Dp}} + \underbrace{\frac{1}{Re}\int_{S_w} \boldsymbol{n}\times\boldsymbol{\omega}\cdot\boldsymbol{i}\,\mathrm{d}A}_{C_{Df}}. \tag{3.3}$$

In general, C_D is summed up by pressure and viscous forces. For inviscid flows, forces applied on a plate are obtained only by pressure forces, and we called this method PFA in this study.

Let us now determine how fluid elements contribute to the drag applied on the finite wing. The uniform incident velocity is $\boldsymbol{c} = \boldsymbol{i}$. The potential flow ϕ_1 in the preceding section is required to satisfy $\nabla\phi_1\cdot\boldsymbol{n} = -\boldsymbol{i}\cdot\boldsymbol{n}$ on the wing, where $\boldsymbol{i}$ is also the unit vector in the drag or thrust direction and $\boldsymbol{n}$ is the normal vector pointing inward from the wing. Let V_R be the volume of fluid enclosed by S_R, which consists of the wing surface S_w and a cuboid surface S_R. Taking inner products with $\nabla\phi_1$ on both sides of (3.1) and integrating over the entire flow region yields

$$\begin{aligned}-\int_{S_w\cup S_R} P\boldsymbol{n}\cdot\nabla\phi_1\,\mathrm{d}A = \int_{S_R}\phi_1\frac{\partial\boldsymbol{v}}{\partial t}\cdot\boldsymbol{n}\,\mathrm{d}A - \int_{V_R}\boldsymbol{v}\times\boldsymbol{\omega}\cdot\nabla\phi_1\,\mathrm{d}V \\ + \frac{1}{Re}\int_{S_w\cup S_R}\boldsymbol{n}\times\boldsymbol{\omega}\cdot\nabla\phi_1\,\mathrm{d}A.\end{aligned} \tag{3.4}$$

Applying the uniform stream condition in the far field and the boundary conditions on the wing body surface, we can carry out the integral on the left-hand side and the first one on the right-hand side with $R\to\infty$ to obtain

$$\underbrace{\int_{S_w} P(\boldsymbol{i}\cdot\boldsymbol{n})\,\mathrm{d}A}_{C_{Dp}} = \underbrace{-\int_V \boldsymbol{v}\times\boldsymbol{\omega}\cdot\nabla\phi_1\,\mathrm{d}V + \frac{1}{Re}\int_{S_w}\boldsymbol{n}\times\boldsymbol{\omega}\cdot\nabla\phi_1\,\mathrm{d}A}_{C_{Dv'}}, \tag{3.5}$$

where V denotes the entire flow region. We call (3.5), in which the pressure force is presented by surface vorticity and volume vorticity forces, VFA, which is defined by $C_{Dv'}$. If the frictional force ($C_{Df} = \int_{S_w}\boldsymbol{n}\times\boldsymbol{\omega}\cdot\boldsymbol{i}\,\mathrm{d}A/Re$) is also included, we have the

drag coefficient on the finite wing:

$$C_D = \underbrace{-\int_V \boldsymbol{v}\times\boldsymbol{\omega}\cdot\nabla\phi_1\,\mathrm{d}V + \frac{1}{Re}\int_{S_w}\boldsymbol{n}\times\boldsymbol{\omega}\cdot\nabla\phi_1\,\mathrm{d}A}_{C_{Dv'}} + \underbrace{\frac{1}{Re}\int_{S_w}\boldsymbol{n}\times\boldsymbol{\omega}\cdot\boldsymbol{i}\,\mathrm{d}A}_{C_{Df}}. \quad (3.6)$$

Also, we rewrite this as

$$C_D = \underbrace{-\int_V \boldsymbol{v}\times\boldsymbol{\omega}\cdot\nabla\phi_1\,\mathrm{d}V}_{C_{Dv}} + \underbrace{\frac{1}{Re}\int_{S_w}\boldsymbol{n}\times\boldsymbol{\omega}\cdot(\nabla\phi_1+\boldsymbol{i})\,\mathrm{d}A}_{C_{Ds}}. \quad (3.7)$$

The first integral, C_{Dv}, on the right-hand side is the force due to the vorticity within the flow. The second integral, C_{Ds}, is the force due to surface vorticity. Meanwhile, we call $-\boldsymbol{v}\times\boldsymbol{\omega}\cdot\nabla\phi_1$ on the right-hand side the volume drag element, and call $\boldsymbol{n}\times\boldsymbol{\omega}\cdot\nabla(\phi_1+\boldsymbol{i})/Re$ the surface drag force element (Chang 1992). Either of these may be termed the vorticity force elements of the drag. A salient feature is that only the volume drag elements near the finite wing contribute significantly to the drag force because $\nabla\phi_1$ is rapidly decaying away from the body. Also, the potential function ϕ_1 can be considered as the geometric factor of the configuration, for each flow condition for a fixed configuration can be associated with a unique ϕ_1.

If we consider the force in lift directions, say $\boldsymbol{j}$, normal to $\boldsymbol{i}$, then ϕ_2 has to satisfy $\nabla\phi_2\cdot\boldsymbol{n} = -\boldsymbol{j}\cdot\boldsymbol{n}$ on the wing surface. The force along the $\boldsymbol{j}$-direction is given by

$$C_L = \underbrace{\int_{S_w} P\boldsymbol{n}\cdot\boldsymbol{j}\,\mathrm{d}A}_{C_{Lp}} + \underbrace{\frac{1}{Re}\int_{S_w}\boldsymbol{n}\times\boldsymbol{\omega}\cdot\boldsymbol{j}\,\mathrm{d}A}_{C_{Lf}}, \quad (3.8)$$

$$C_L = \underbrace{-\int_V \boldsymbol{v}\times\boldsymbol{\omega}\cdot\nabla\phi_2\,\mathrm{d}V + \frac{1}{Re}\int_{S_w}\boldsymbol{n}\times\boldsymbol{\omega}\cdot\nabla\phi_2\,\mathrm{d}A}_{C_{Lv'}} + \underbrace{\frac{1}{Re}\int_{S_w}\boldsymbol{n}\times\boldsymbol{\omega}\cdot\boldsymbol{j}\,\mathrm{d}A}_{C_{Lf}} \quad (3.9)$$

$$= \underbrace{-\int_V \boldsymbol{v}\times\boldsymbol{\omega}\cdot\nabla\phi_2\,\mathrm{d}V}_{C_{Lv}} + \underbrace{\frac{1}{Re}\int_{S_w}\boldsymbol{n}\times\boldsymbol{\omega}\cdot(\nabla\phi_2+\boldsymbol{j})\,\mathrm{d}A}_{C_{Ls}}. \quad (3.10)$$

Likewise, $-\boldsymbol{v}\times\boldsymbol{\omega}\cdot\nabla\phi_2$ is called the volume lift element, and $\boldsymbol{n}\times\boldsymbol{\omega}\cdot\nabla(\phi_2+\boldsymbol{j})/Re$ is called the surface lift force element. It is noted that we should have $C_{DP} = C_{Dv'}$ (and $C_{LP} = C_{Lv'}$) provided that the Navier–Stokes equations are exactly solved. In practice, they are not identical because there are always numerical errors; and therefore their agreement with each other serves as a check of numerical accuracy.

4. Results and discussion

The present force representation will be applied to the flow around finite plates of aspect ratios $AR = 1$, 2, 3, with particular emphasis on the effects of the lift and drag elements. The AoA varies in the range from 5 to 60°, while the Reynolds numbers considered include 100 and 300.

4.1. *Numerical method and validation of results*

The numerical results are obtained by solving the Navier–Stokes equations using the Simple C method of the commercial code FLUENT based on the control-volume

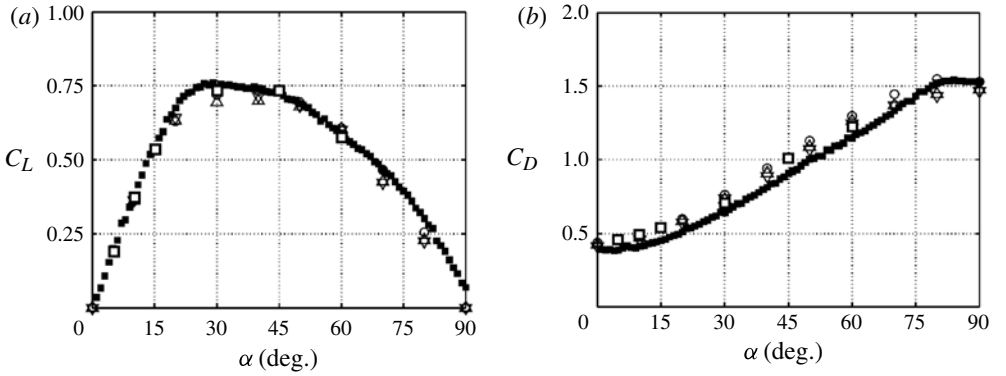

FIGURE 2. (*a*) Steady state of lift and (*b*) drag coefficients for a rectangular plate of $AR = 2$ at $Re = 100$ obtained from experiments (■) and numerical simulations with different grid size based on pressure-frictional forces (○, △ and ▽), i.e. Taira & Colonius 2009, as well as the force representation (□). It is noticed that the former authors define $C_D = 2D^*/\rho U^2 A$ and $C_L = 2L^*/\rho U^2 A$, and therefore the present coefficients are multiplied by a factor of two to have the comparisons on the same base.

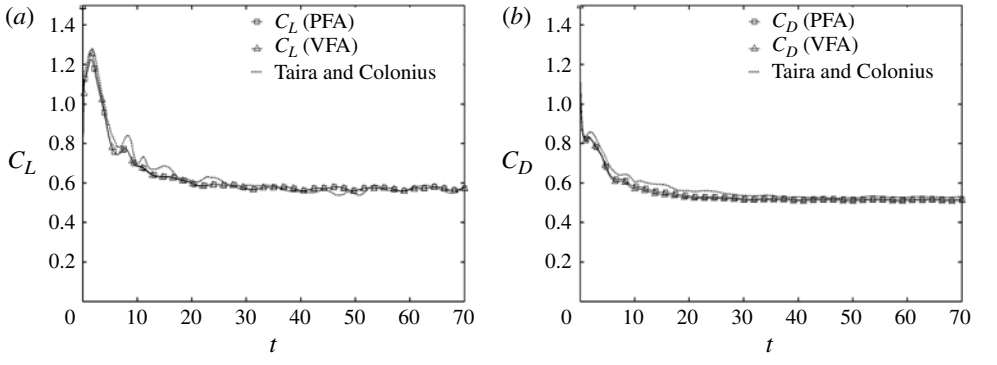

FIGURE 3. (*a*) Time histories of the total lift coefficients and (*b*) time histories of the total drag coefficients for the $AR = 1$ plate at $\alpha = 30°$ with $Re = 300$ obtained by PFA and VFA compared with the results (dashed line) of Taira & Colonius (2009).

method. A second-order up-wind scheme is applied to spatial discretization, while time integration is implemented by using a first-order implicit scheme. The far-field boundary conditions consist of a uniform flow (U_∞) in the inlet and the pressure outlet condition. The Courant number is always required to satisfy $U_\infty \Delta x/\Delta t < 0.5$. Numerical simulations are carried out in a rectangular box of length 26 (streamwise) × width 14 (spanwise) × height 12 (vertical). The thickness of the plate is 0.037. The grid size for the case of $AR = 2$ ranges from 150 to 180 million points with the smallest resolution $\delta_x = 0.016$. In $AR = 3$ case, the domain with larger width length is used for simulations.

Selected numerical results are compared with those of Taira & Colonius (2009) for ensuring their accuracy; these include the steady lift and drag force coefficients for the plate of $AR = 2$ at $Re = 100$, and the transient lift and drag coefficients for $AR = 2$ at $Re = 300$. Figure 2 shows the comparisons of the steady lift and drag force coefficients for the plate of $AR = 2$ at $Re = 100$ at AoA of 5, 10, 15, 30, 45 and 60°. The results are in close agreement with each other. Figure 3 shows the comparisons of the time

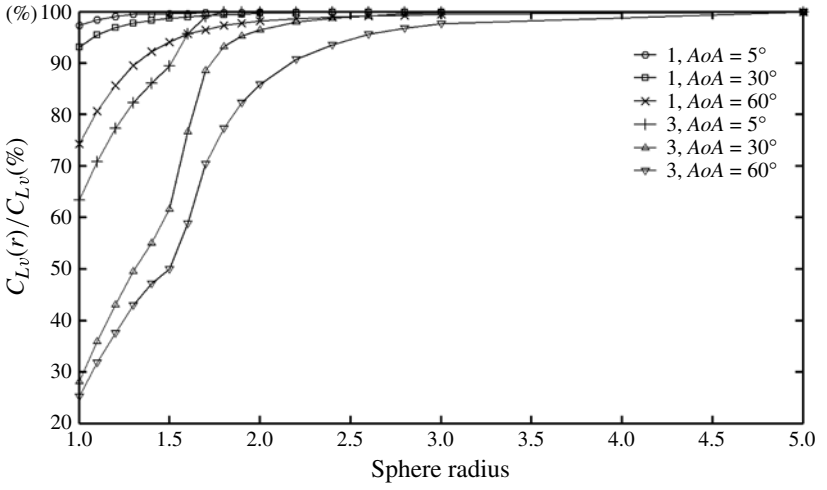

FIGURE 4. Accumulation of the lift elements of C_{Lv} in percentage: $C_{Lv}(r)/C_{Lv} \times 100\,\%$, where $C_{Lv}(r) = -\int_{|\boldsymbol{x}|\leqslant r} \boldsymbol{Lv} \times \boldsymbol{\omega} \cdot \nabla\phi_2 \,\mathrm{d}V$, $r = 1 \sim 5$.

histories of the unsteady lift and drag coefficients for the plate of $AR = 2$ at $Re = 300$ and AoA of 30° from $t = 0$–70 where we computed the forces by both PFA and VFA approaches. It is shown that the lift and drag coefficients obtained by PFA and VFA are almost the same, while they are slightly different compared with the numerical results of Taira & Colonius (2009). This might be due to difference in the thickness of the flat plate. In the work of Taira & Colonius (2009), the plate is infinitely thin, while in our setting the thickness is 0.037 as mentioned above.

Next, it is noted that we have sufficient accuracy by performing the integration in (3.7) and (3.10) within two or three chord lengths of the plate. This is because the integrands (force elements) are rapidly decaying away from the plate. As the diameter of the computational domain is at least 10 times the chord length of the plate. These facts indicate that the wake vortices have no contribution to the forces as they are leaving the computational domain. As an illustration, figure 4 shows the accumulated distributions of C_{Lv}-volume vorticity lift coefficient along the radial direction (from $r = 1$ to 5) at $t = 20$ for the plate of different aspect ratios at various AoAs. It can be seen that the convergence is faster for the LAR plates at lower AoAs, and is slower for the high-aspect-ratio plates at higher AoAs. Nevertheless, in all of the cases under consideration the convergence reaches 99 % within three chord lengths of the plate.

4.2. *The force representation for the $AR = 1$ plate at different AoAs*

To start with the discussion, we consider an impulsively started flow over a finite wing of $AR = 1$ for $Re = 300$, in which the tip effects are more significant. Figure 5(*a–f*) shows the time histories of the total lift and drag coefficients (C_L and C_D) and its various force components at six AoAs. Taira & Colonius (2009) have a very interesting observation the two-dimensional time-average lift-to-drag ratio reaches its maximum around 10°, while that of $AR = 1$ is achieved near $\alpha = 20°$. They suggested that favourable operating conditions at higher AoAs for the LAR wings. In this study, we also consider $\alpha > 20°$ as a high AoA. It is noted that as the AoA is larger than 20°, the trends of both total lift and drag coefficients C_L and C_D are similar, attaining a local maximum after the impulsive start maintaining the value to $t \sim 2$ then gradually

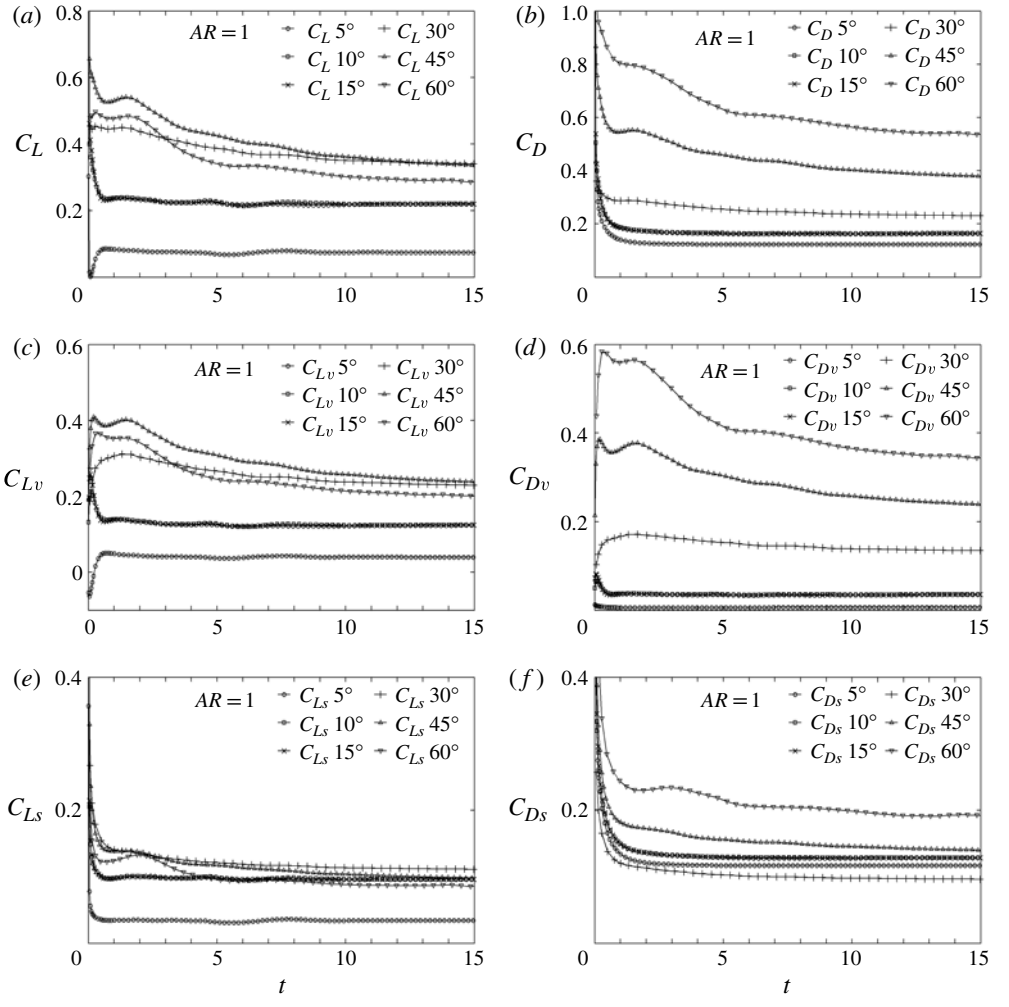

FIGURE 5. Time histories of various lift and drag coefficients for the $AR = 1$ plate at six different AoAs with $Re = 300$.

decaying to a stable value. The lift coefficient C_L drops quickly in an initial period, then rises to its maximum ($t \sim 1$–3), and then decreases gradually to a stable value after $t \sim 10$. Note that the local maximum lift coefficient is the largest at $\alpha = 45°$. For the case with an AoA of 60°, the lift coefficient C_L initially lies between the two cases $\alpha = 30°$ and $\alpha = 45°$ then decreases to lie below both after $t \sim 3$. For the $AR = 1$ plate with lower AoAs ($\alpha < 20°$), it is found that the behaviours of C_L in the cases of $\alpha = 10$ and 15° are similar to each other: C_L starts from a large value, decreases to a stable value (=0.24) at $t \sim 0.5$, and maintains it to large t. In the $\alpha = 5°$ case, initially, C_L drops sharply to zero and then increases to a stable value 0.08 from $t \sim 0.5$ to late time. It is noted that the total lift for the high AoA cases is obviously larger than those for the low AoA cases. These above behaviours in C_L are also similar to the results obtained by Taira & Colonius (2009). A further look at the lift C_L represented by the components due to volume vorticity (C_{Lv}) and surface vorticity (C_{Ls}) shows that at large α (>20°), C_{Ls} starts from a very large value right after the impulsive

start and drops to the value 0.15, while C_{Lv} increases from nearly zero to a value between 0.3 and 0.4 around $t \sim 0.001$. After the impulsive start, a notable behaviour is that C_{Ls} maintains a stable positive value (=0.10) for a long time. It should also be noted that C_{Lv} contributes to the lift most significantly at $\alpha = 45°$, then in order at 30°, 60°, which is identical to the total lift coefficient C_L. This means that the variation of total lift is strongly dependent on the volume vorticity C_{Lv}. However, for the AoA of 15° case, as time increases, C_{Lv} and C_{Ls} have almost equal contributions to the total lift C_L, which means that C_{Lv} and C_{Ls} are both significant at low AoAs for low-Reynolds-number flows. For the low α cases, the trends of C_{Lv} and C_{Ls} for AoAs of 15 and 10° cases are identical. In comparison, C_{Lv} and C_{Ls} for an AoA of 5° are much smaller. It is interesting to note that C_{Ls} finally attains a stable value of 0.10–0.14 for all of the cases under consideration except for $\alpha = 5°$.

Next, we consider the time histories of the total drag coefficient (C_D) and its corresponding components for $AR = 1$ with different AoAs. At a higher AoA ($\alpha \geqslant 20°$), it drops sharply after an impulsive start, varies slightly around a large value ($t \sim 1$–2), and then decreases slowly to a fairly constant value for all cases. This was also observed numerically by Taira & Colonius (2009) at the AoAs from 20 to 60°, and experimentally by Kim & Gharib (2010) and Ringuette *et al.* (2007) for $\alpha = 90°$ at higher Reynolds numbers. Nevertheless, at a lower AoA ($\alpha < 20°$) C_D decreases sharply in an initial period up to $t = 0.5$, and then maintains a stable value for a long time. The trends of C_D for $\alpha = 10$ and 15° are almost the same. The total drag coefficient C_D also can be examined by representing them in terms of C_{Ds} and C_{Dv}. For all α, the component C_{Ds} decreases sharply from a large value in a short initial period and decreases slowly to a stable value at late time. In contrast C_{Dv} rises rapidly from zero in the beginning and maintains a large value at a higher α; one maximum and one local maximum exist for two cases of $\alpha = 45$ and 60° in an initial time interval [0.5, 2.5]. In contrast, for a lower α ($\alpha = 10$ and 15°), C_{Dv} increases in a short initial time, decreasing sharply around $t \sim 0.5$ and remains at that value (∼0.05). In addition, it is shown that all of the values of C_D and C_{Dv} increase with increasing the AoA of the plate. However, C_{Ds} in the case of $\alpha = 30°$ is the smallest of all of the cases.

How do the forces exerted upon the plate relate to the three-dimensional wake vortices, in particular, TiVs, LEVs and trailing-edge vortices (TEVs)? Let us sample some time instants, and investigate the vorticity distribution and volume lift elements. We first choose to study the evolution and formation of vortex structures for the $AR = 1$ plate of with $\alpha = 45°$ and $Re = 300$. In the following, we show the snapshots of the velocity gradient tensor, known as the Q-value or Q-criterion, at different times, highlighting the lift force elements with different colours to exhibit the unsteady mechanisms of various flow structures. The Q-value proposed by Hunt, Wray & Moin (1988) is defined as $Q \equiv 1/2(\|\boldsymbol{\Omega}\|^2 - \|\boldsymbol{S}\|^2)$, where $\boldsymbol{\Omega} \equiv 1/2[\nabla \boldsymbol{v} - (\nabla \boldsymbol{v})^{\mathrm{T}}]$ and $\boldsymbol{S} \equiv 1/2[\nabla \boldsymbol{v} + (\nabla \boldsymbol{v})^{\mathrm{T}}]$. The flow wake visualized by means of Q-value is an easy way to understand the vortex structure and identify the coherent structures of the flow.

Figure 6(*a*) shows the flow field at the early time $t = 0.072$ with the isosurface of $Q = 3$, for which a positive value means that vorticity prevails over strain. At this moment, strong vorticity in vortices with positive lift elements are generated around the whole edges of the plate, resulting in the rapid increase in C_{Lv} (see figure 5*c*). Figure 6(*b*) shows three slices of x–y plane coloured by volume lift elements at the spanwise positions $z = 0$ and ±0.4. It is also found that two strong shear layers occur on the top and bottom of the plate right just after the impulsive start. These two regions of opposite and strong vorticity around a translating and flapping wing are

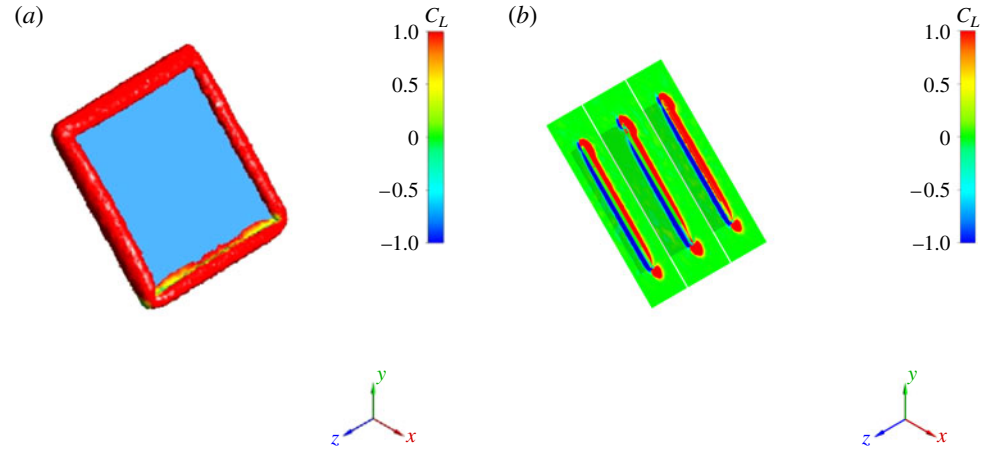

FIGURE 6. (Colour online available at journals.cambridge.org/flm) Flow visualizations for the $AR = 1$ plate with $\alpha = 45°$, $Re = 300$ at $t = 0.072$: (*a*) the topology of Q value $= 3$; (*b*) three slices over the wing plate coloured by the volume lift elements at the spanwise positions $z = 0$ and ± 0.4.

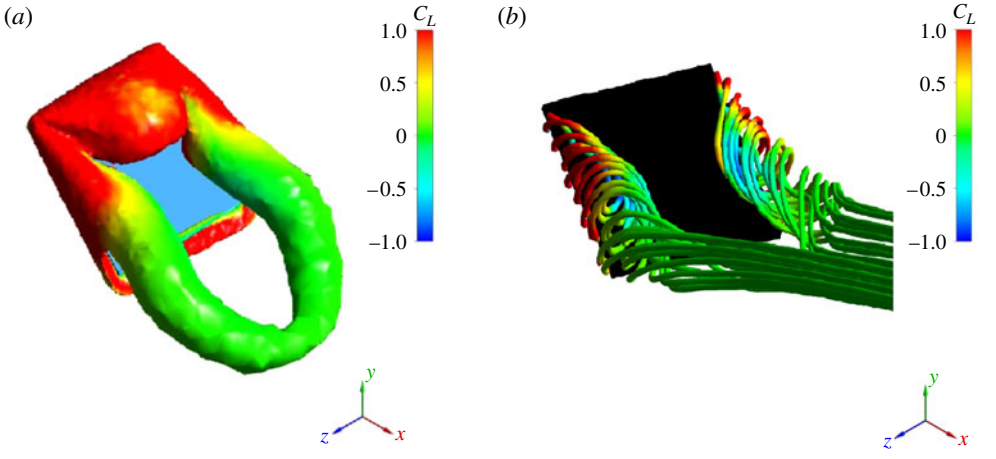

FIGURE 7. (Colour online) Flow visualizations for the $AR = 1$ plate with $\alpha = 45°$, $Re = 300$ at $t = 1.40$: (*a*) the topology of Q value $= 3$; (*b*) a streamline of the TiVs coloured by the volume lift elements.

also observed by Birch, Dickson & Dickinson (2004). The one on the top generates positive lift elements, while the one on the bottom provides negative lift elements. Thereafter, the flow continues to develop and rolls up to form LEVs, TEVs and TiVs as the generated vorticity is being fed in the flow (figure 7*a*). At the instant $t = 1.4$, the part of LEV which is close to the midspan attaches on the upper side of the plate. Also, the LEV structure is anchored to the front corners of the plate due to the suppression by the TiVs and forms an arching shape. This was observed in smoke visualizations conducted by Freymuth, Bank & Finaish (1987). In general, the LEV provides large positive lift elements to the plate. This is also called dynamic stall from the viewpoint of vorticity force responsible for lift enhancement, when a low pressure

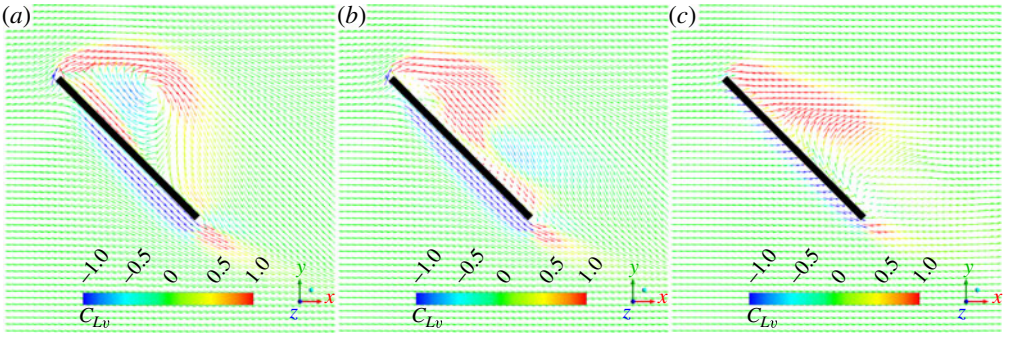

FIGURE 8. (Colour online) The x–y plane velocity vectors coloured by the volume lift elements at various spanwise locations for the $AR = 1$ plate with $\alpha = 45$, $Re = 300$ at $t = 1.40$: (*a*) $z = 0$; (*b*) $z = 0.3$; (*c*) $z = 0.5$.

exists in the core of the LEV (Maxworthy 1979; Ellington *et al.* 1996). In our previous studies, this mechanism was also identified for insect flapping (Hsieh *et al.* 2009).

We now turn to a discussion of TiVs. Interestingly, a conical TiV structure develops across each of the two chord sides, where the apex of each TiV is located at the upper front right-angled corner of the plate. These two TiVs join with the LEV at the two front corners. From the distribution of lift elements, the apex of each TiV (the newly generated structure with strong vorticity) contributes positive lift. However, some parts of the TiVs are shed to the back upper corner of the plate, the positive strength in lift diminishes rapidly because the vorticity diffuses, and their distances to the plate increase. Recall that only the vorticity elements near the plate contribute significantly to the force because $\nabla\phi$ is decaying away from the plate with $1/r^3$. The LEVs, TEVs and TiVs interweave with each other to form a system of closed vortices (like a vortex ring). It is found that these shed, closed vortices with spanwise-direction vorticity have a near-zero contribution to the lift of the plate. Meanwhile, the thin layer of vortex sheet (the newly generated TEVs), consecutively generated from the trailing edge of the plate, provides some positive lift elements. Figure 7(*b*) shows the velocity streamlines of the TiVs generated at the two side edges of the plate. The varied colour of the streamlines indicates the different lift-element strengths. It is found that the pair of TiVs provides positive lift elements as they roll up from below to above the plate. As the TiVs turn around and move toward the plate, their strengths decay, giving negative lift contributions. After the TiVs advects downstream from the plate, the lift contribution of the TiVs is vanishing.

Next, we show in figure 8(*a–c*) the velocity profiles coloured by the volume lift elements at three spanwise locations $z = 0$ (midspan), 0.3 and 0.5 (the plate edges). At the midspan ($z = 0$), we see that the developing LEV, in which the flow reattaches to the upper side of the plate and forms a separation bubble, giving a net positive contribution to the lift. At the cross-section $z = 0.3$, the TiVs have an obvious impact on the structure of the LEV: the strong downwash velocity of the TiVs presses the velocity of the LEV to parallel the plate. The regions where the LEV and TiVs interlink produce large positive lift elements. This is a totally different perspective that identifies the mechanism of TiVs is possible for lift generation. Previous studies (e.g. Shyy *et al.* 2010) had concluded that the downward velocity may be regarded as a cause of reduced lift. At the side edges ($|z| = 0.5$), the TiVs almost completely control the nearby velocity field, and as a result the separation bubble does not

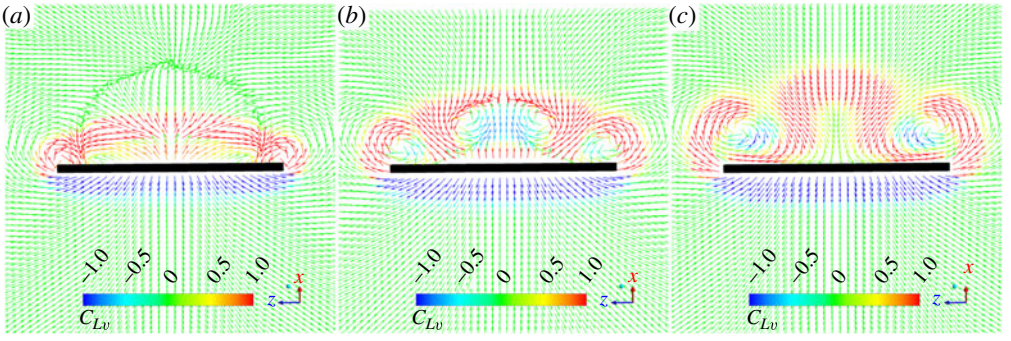

FIGURE 9. (Colour online) The y–z plane velocity vectors coloured by the volume lift elements at various chordwise locations for the $AR = 1$ plate with $\alpha = 45$, $Re = 300$ at $t = 1.40$: (*a*) $x = 0.14$; (*b*) $x = 0.35$; (*c*) $x = 0.57$.

exist. Obviously, the initial generation of the TiVs is full of positive lift elements. Figure 9(*a–c*) shows the velocity profiles on the y–z plane coloured by volume lift elements at the chordwise directions $x = 0.14$, 0.35 (near midchord) and 0.57. From the velocity profile, the TiVs with the positive lift elements are easy to visualize. It is shown that the newly generated vorticity from all of the edges of the plate provides large positive lift elements (see, e.g., the LEV in figure 9*b* and all of the TiVs). The velocity field of the LEVs at the midspan ($z = 0$) is mainly upward, yet there is a downward flow due to the influence of the TiVs at $z = \pm 0.25$. It is noted that from figures 8 and 9 that the flow passing just below and along the plate contributes negative lift elements (blue).

As time evolves to $t = 2.28$, the previously formed vortex ring structure advects downstream, and its overall strength weakens (see figure 10*a*). At this moment, the LEV is ready to pinch off and advect downstream, almost extending over the entire upper plate. A similar behaviour was also reported by Taira & Colonius (2009) and Kim & Gharib (2010). The pinch-off LEV and vortex ring which advects downstream the plate has small lift contribution on lift generation for the plate (green). However, the arching LEV remains close to the front corners due to interaction with the TiVs, which leads to most lift elements being attached to the leading edge and prevents a rapid loss in the lift due to the LEV separation. Also, the lift elements generated near the apex of the TiVs contribute significantly large positive lift elements. The LEV attached to the plate is due to the downward induced velocity from the TiVs (Taira & Colonius 2009; Shyy *et al.* 2010). Figure 10(*b*) represents the flow field at $t = 5.7$ when, the whole vortex ring and TiVs grow larger. In addition, the leading-edge vortex forms a horse-shoe vortex above the plate with the two side vortex tubes growing longer and lining up in parallel. These vortices have weaker influences on the lift force exerted on the plate. All of the sources of lift elements for the plate mainly come from the newly generated vorticity around the edges of the plate, shown in figure 10(*b*).

Some snapshots of velocity gradient tensor ($Q = 3$) coloured by lift elements for the case of $AR = 1$ at $\alpha = 15°$ ($t = 0.77$) and 60° ($t = 1.89$) are shown in figure 11(*a,b*). The vorticity especially in the LEV and the parts of the TiVs round the front corners of the plate, generated initially around the plate, has a large positive contribution to the lift. Also, the newly generated vorticity at the front corners of the plate for these two cases contain largely positive lift elements. As the vortex ring advects to the far wake, its strength decays and contributes little to the lift.

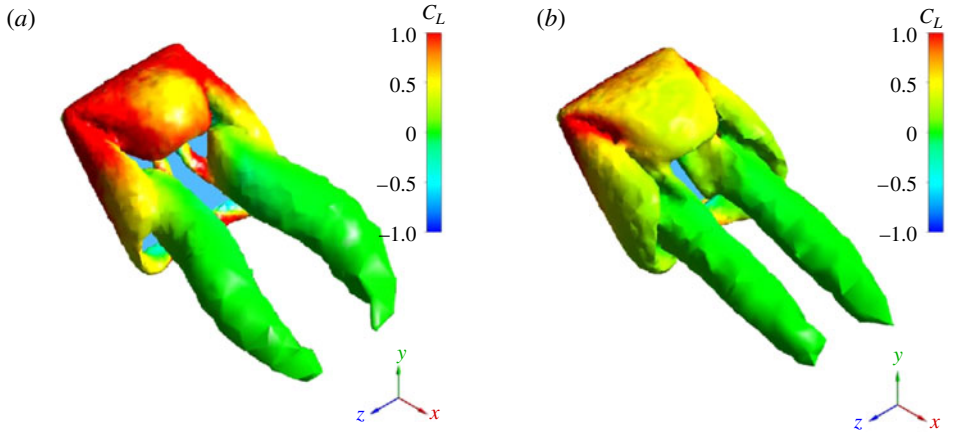

FIGURE 10. (Colour online) Flow visualizations for the $AR = 1$ plate with $\alpha = 45°$, $Re = 300$ at (*a*) $t = 2.28$ and (*b*) 5.70.

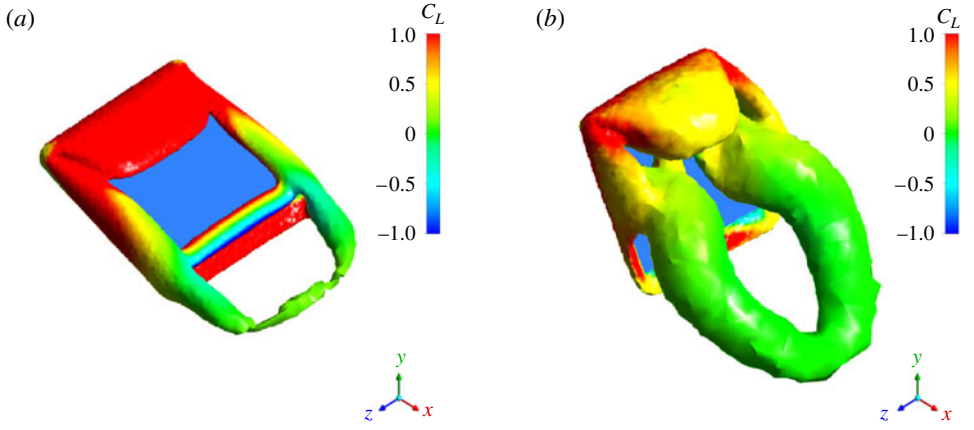

FIGURE 11. (Colour online) The topology of Q value $= 3$ coloured by the volume lift elements for the $AR = 1$ plate with $Re = 300$ at (*a*) $\alpha = 15°$, $t = 0.77$ and (*b*) $\alpha = 60°$, $t = 1.89$.

In summary, the above results reveal four regions of lift elements responsible for the transient variation of the lift coefficient after the impulsive start. The first is the LEV generated and attached to the leading edge of the plate, accumulating large positive lift elements. The second is due to the strong TiVs, which the fluid elements roll up from below to above the plate have a large positive contribution to the lift. The third is the strong interaction between the LEV and TiVs, which exists only in the middle part of the front edge of the plate. The fourth is the negative lift elements in the slender region below and along the plate. As long as a vortex structure diffuses and advects away from the plate, it no longer makes an important contribution to the lift on the plate.

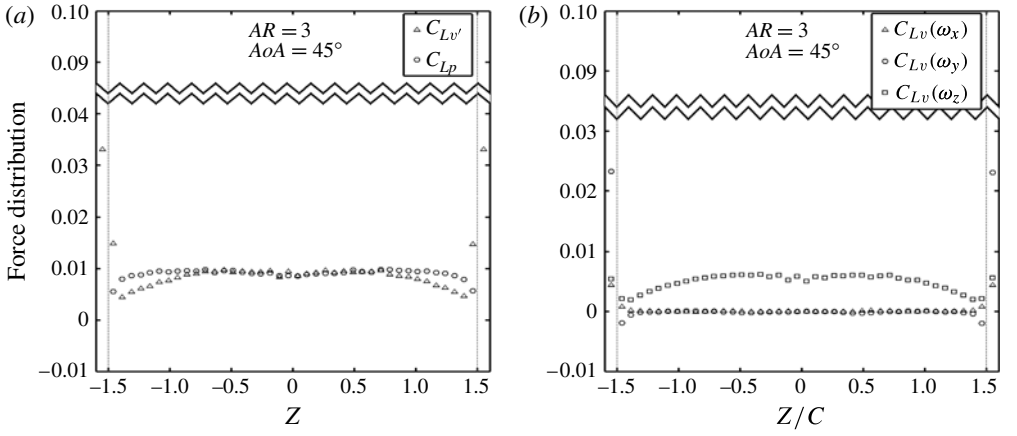

FIGURE 12. (*a*) Sectionwise distributions of $C_{Lv'}$ (with values along the plate as well as in the two outer regions) and C_{Lp} (with values only along the plate); (*b*) sectionwise distributions of the volume vorticity lift components $C_{Lv}(\boldsymbol{\omega_x})$, $C_{Lv}(\boldsymbol{\omega_y})$ and $C_{Lv}(\boldsymbol{\omega_z})$ for the $AR = 3$ plate with $\alpha = 45°$, $Re = 300$ at $t = 20.0$.

4.3. *Three-dimensional flow characteristics by pressure force analysis and vorticity force analysis*

4.3.1. *Sectional pressure force distribution and vorticity force distribution*

In order to view the behaviours that distinguish three-dimensional flow from two-dimensional flow, we examine the force distributions along the spanwise direction in terms of both pressure force and force elements. Along the spanwise direction, we divide the whole flow space into 42 regions by 41 equally spaced parallel planes vertical to the finite wing; 40 of them contain a section of the finite wing, and 2 are the rightmost and leftmost outer regions. Given a force component (lift or drag): (i) we first calculate the pressure force for each of the 40 sections (this gives a lift or drag distribution along the spanwise direction $C_{Lp}(z)$ or $C_{Dp}(z)$); (ii) we then calculate the sum of vorticity force elements (of $C_{Lv'}(z)$ for lift or $C_{Dv'}(z)$ for drag) over each of the 42 regions (this also gives a lift or drag distribution along the spanwise direction $C_{Lv'}(z)$ or $C_{Dv'}(z)$). It is appropriate to call (i) the PFA and (ii) the VFA. The contributions in the spanwise section for these two viewpoints are called sectional pressure force (SPF) and sectional vorticity force (SVF), respectively. The base of comparison is thus: in a truly two-dimensional flow (necessarily over a wing of infinite span), we do not have two outer regions and the two force distributions calculated by (i) and (ii) must be identical, i.e. $C_{Lp}(z) = C_{Lv'}(z)$ and $C_{Dp}(z) = C_{Dv'}(z)$. However, in the three-dimensional case, the two distributions from two different perspectives give different insights into the force contributions. Let us consider force distributions at two distinct moments: one at an early stage of flow development and one at a later time. First let us consider the instant $t \sim 13$ the force coefficients decay to a stable value. In the case of a wider span (say, $AR = 3$), we expect that in the middle sections, the two force distributions will be closer to each other, and near the edges they deviate from each other; the discrepancy is made up by the force element in the two outermost regions. This is indeed the case, as shown in figure 12(*a*). Note that $C_{Lp}(z)$ at the central section is slightly smaller than at the neighbouring sections but decreases toward the two side edges of the finite wing. Here, z lies between $\pm AR/2$. As a comparison, $C_{Lv'}(z)$ is closer to $C_{Lp}(z)$ in the middle part between $z = \pm 0.6$,

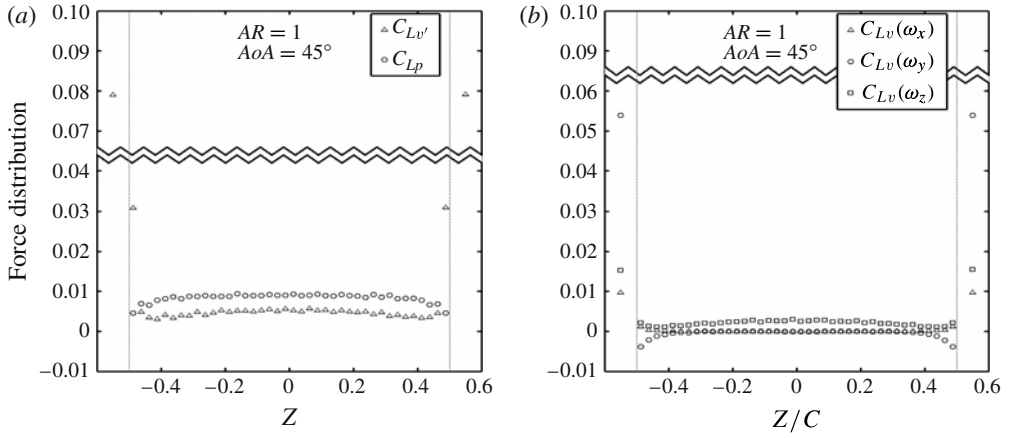

FIGURE 13. (*a*) Sectionwise distributions of $C_{Lv'}$ (with values along the plate as well as in the two outer regions) and C_{Lp} (with values only along the plate); (*b*) sectionwise distributions of the volume vorticity lift components $C_{Lv}(\boldsymbol{\omega_x})$, $C_{Lv}(\boldsymbol{\omega_y})$ and $C_{Lv}(\boldsymbol{\omega_z})$ for the $AR = 1$ plate with $\alpha = 45°$, $Re = 300$ at $t = 20.0$.

and then becomes smaller than $C_{Lp}(z)$ farther away from the midspan, but exceeds $C_{Lp}(z)$ at the two edge regions, and has a significant value in the two outer regions. In the case of LAR ($AR = 1$), the flow is more three-dimensional. There are few places where the three-dimensional flow resembles the two-dimensional flow. The TiVs interact closely with the LEVs and TEVs, and it is impractical and less meaningful to separate them as individual objects. We shall return to the point of making distinctions between the force contribution from the various vortices in § 4.3. One signature of the three-dimensional flow is illustrated by figure 13(*a*), which shows that $C_{Lv'}(z)$ is most substantial smaller than $C_{Lp}(z)$ in most of the regions, but is significantly compensated for by the two edge regions, and remarkably by the two outermost regions. The comparison shows that the relative importance of the outer TiVs is especially significant for LAR wings.

Next, we consider the early stage of flow development. Right after the flow is started, vorticity is generated intensely around the finite wing as well as in the two outer regions of TiVs. Figure 14(*a*) shows the case for $AR = 3$, which provides an interesting comparison between $C_{Lp}(z)$ and $C_{Lv'}(z)$ at the early $t = 0.46$. In the middle sections ($-0.75 \leqslant z \leqslant 0.75$), $C_{Lv'}(z)$ is a little larger than $C_{Lp}(z)$, being closest to $C_{Lp}(z)$ near the middle part $z = \pm 0.75$, and decreases rapidly toward the two edges of the plate. Also, the sectionwise discrepancy between $C_{Lp}(z)$ and $C_{Lv'}(z)$ is mainly made up by the force elements of the TiVs in the outermost and outer regions. It is noted that $C_{Lv'}(z)$ has a larger value (0.064) at an early time than that (=0.034, see figure 12*a*) at late time $t = 20$. We also consider the case of LAR $AR = 1$ at $t = 1.56$ (see figure 15*a*). $C_{Lv'}(z)$ is totally different from $C_{Lp}(z)$ at this instant. The maximum of $C_{Lp}(z)$ no longer exists in the midspan but is found at $z = \pm 0.3$. $C_{Lp}(z)$ declines from $z = \pm 0.3$ to the two edges and to the midspan. This decrease in $C_{Lp}(z)$ is due to the downwash flow, according to traditional aerodynamic theory. However, $C_{Lv'}(z)$ has the local maximum (=0.013) at $z = \pm 0.2$ and varies violently, while its values are smaller than $C_{Lp}(z)$ along the most of the span (except for the outermost section of the plate). The large $C_{Lv'}(z)$ occurs at the two outer regions and the outermost sections (=0.085 and 0.052, respectively). It is concluded that at the early stage of

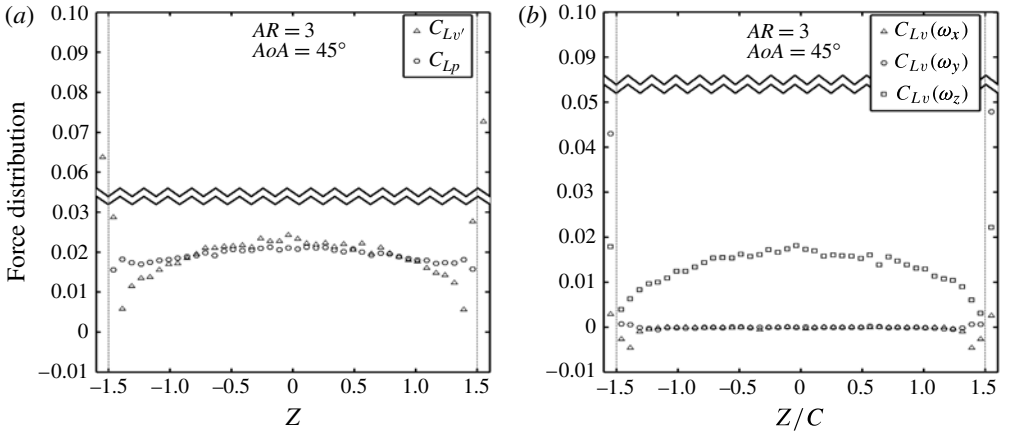

FIGURE 14. (*a*) Sectionwise distributions of $C_{Lv'}$ (with values along the plate as well as in the two outer regions) and C_{Lp} (with values only along the plate); (*b*) sectionwise distributions of the volume vorticity lift components $C_{Lv}(\boldsymbol{\omega_x})$, $C_{Lv}(\boldsymbol{\omega_y})$ and $C_{Lv}(\boldsymbol{\omega_z})$ for the $AR = 3$ plate with $\alpha = 45°$, $Re = 300$ at $t = 0.46$.

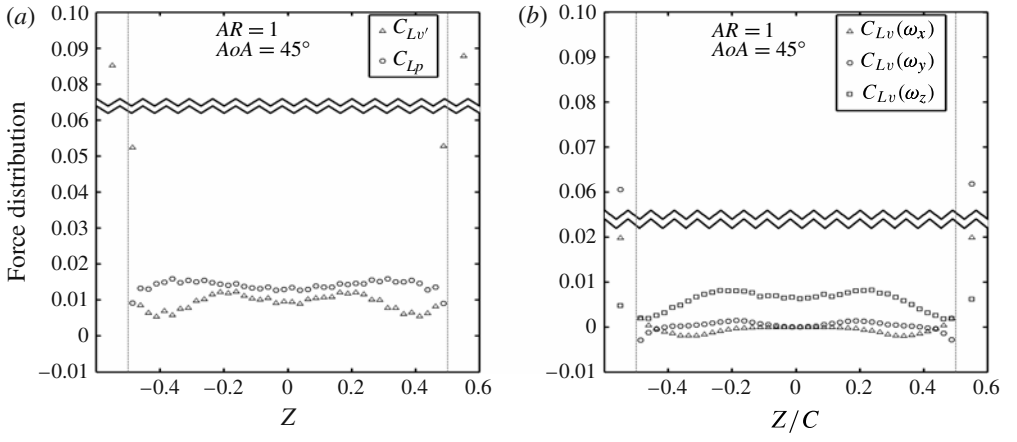

FIGURE 15. (*a*) Sectionwise distributions of $C_{Lv'}$ (with values along the plate as well as in the two outer regions) and C_{Lp} (with values only along the plate); (*b*) sectionwise distributions of the volume vorticity lift components $C_{Lv}(\boldsymbol{\omega_x})$, $C_{Lv}(\boldsymbol{\omega_y})$ and $C_{Lv}(\boldsymbol{\omega_z})$ for an $AR = 1$ plate with $\alpha = 45°$, $Re = 300$ at $t = 1.56$.

flow development, the intense a TiVs are significant in promptly providing positive lift elements before the LEV is further developed.

Brief remarks concerning the distinctions between the VFA and PFA are made available from the above observations. (*a*) The vorticity force viewpoint provides us with a base for relating vorticity directly to the force, with clearly defined information of how and where (in which regions) the finite wing loses the capacity to gain lift, as in the two-dimensional flow, and to what capacity the finite wing can gain and win back lift from the outer regions of TiVs. (*b*) In terms of flow control, the pressure force viewpoint indicates where the surface pressure should be optimized by modifying the shape and its motion of the wing surface. On the other hand, the

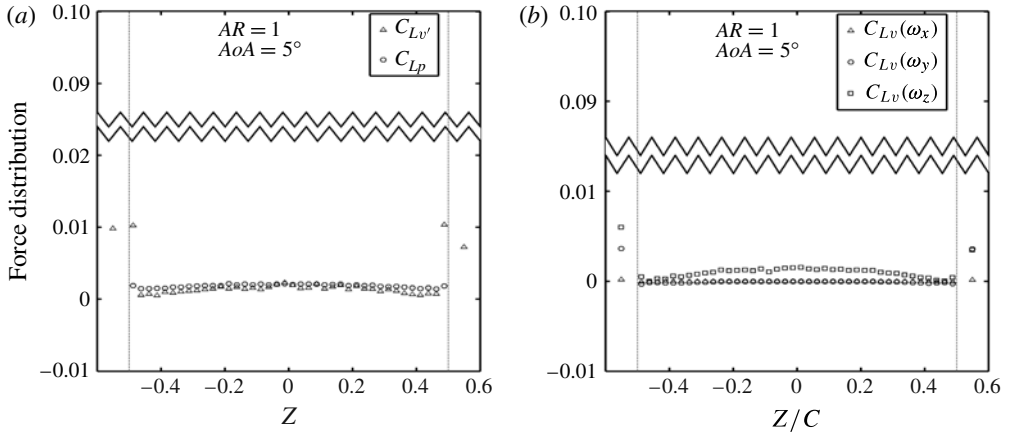

FIGURE 16. (*a*) Sectionwise distributions of $C_{Lv'}$ (with values along the plate as well as in the two outer regions) and C_{Lp} (with values only along the plate); (*b*) sectionwise distributions of the volume vorticity lift components $C_{Lv}(\boldsymbol{\omega_x})$, $C_{Lv}(\boldsymbol{\omega_y})$ and $C_{Lv}(\boldsymbol{\omega_z})$ for the $AR = 1$ plate with $\alpha = 5°$, $Re = 300$ at $t = 0.72$.

vorticity force viewpoint indicates in which regions the vorticity can be manipulated by modifying the wing shape and its motion to most effectively enhance its force contribution to the force. Any vorticity in the flow may influence the pressure in any flow point; however, this is not the most useful point of the approach and is not pursued here. It is most useful to relate vorticity directly to force.

4.3.2. *Relative force contributions from transverse vorticity components* $\boldsymbol{\omega_x}$, $\boldsymbol{\omega_y}$

Important three-dimensional characteristics of the flow field could further be pursued along the line of VFA by investigating the relative importance of the volume-vorticity force components. In the following, the individual components of the lift coefficient due to the vorticity $\boldsymbol{\omega_x}$, $\boldsymbol{\omega_y}$ and $\boldsymbol{\omega_z}$ are denoted by $C_{Lv}(\boldsymbol{\omega_x})$, $C_{Lv}(\boldsymbol{\omega_y})$ and $C_{Lv}(\boldsymbol{\omega_z})$, respectively. The same convention applies to the drag coefficients: the respective drag components are denoted by $C_{Dv}(\boldsymbol{\omega_x})$, $C_{Dv}(\boldsymbol{\omega_y})$ and $C_{Dv}(\boldsymbol{\omega_z})$. An important characteristic is the influence range of TiVs, which is defined to be the proportion of the plate span over which $C_{Lv}(\boldsymbol{\omega_x})$ or $C_{Lv}(\boldsymbol{\omega_y})$ ($C_{Dv}(\boldsymbol{\omega_x})$ or $C_{Dv}(\boldsymbol{\omega_y})$) deviates substantially from zero. We consider that the flow has a stronger three-dimensional character wherever the z-component varies more violently along the plate span or the relative importance of the x- or y- force components to the z-component is increased. As a matter of fact, the variation of volume-vorticity forces, including the contributions from the TiVs, is highly dependent on three factors: AoA, time and aspect ratio. First we consider the lift for the cases of lower AoA. Figures 16(*b*) and 18(*b*) show the distributions of three volume vorticity lift components along the spanwise direction for the $AR = 1$ plate at $\alpha = 5$ and 15°, respectively. At the early stages ($t = 0.72$ for figure 16*b*; $t = 1.17$ for figure 18*b*), the part of $C_{Lv}(\boldsymbol{\omega_z})$ closer to the midspan is obviously higher than those near the two sides edges. In contrast, the parts of $C_{Lv}(\boldsymbol{\omega_x})$ and $C_{Lv}(\boldsymbol{\omega_y})$ closer to the midspan are almost zero, but becoming slightly negative toward the two side edges (between $|z| = 0.4$ and 0.5). Interestingly, we note the strong tip effects generated in two outer regions where $C_{Lv}(\boldsymbol{\omega_y})$ contributes a positive lift to the plate, and the contribution even exceeds that provided by $C_{Lv}(\boldsymbol{\omega_z})$ as AoA increases. As a comparison, at the lower AoA $\alpha = 5°$, we have $C_{Lv}(\boldsymbol{\omega_z})$ (=0.0061), $C_{Lv}(\boldsymbol{\omega_y})$ (=0.0037), $C_{Lv}(\boldsymbol{\omega_x})$ (=0.0004) in the decreasing order of magnitude, while at the higher AoA

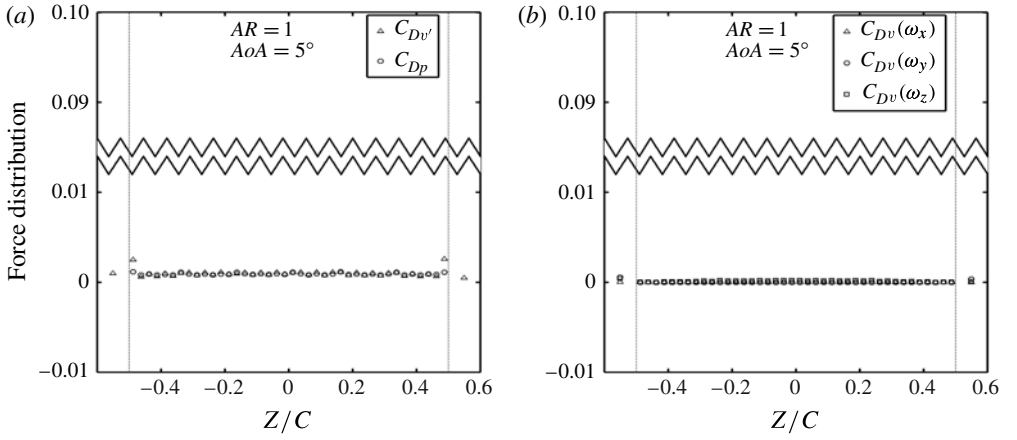

FIGURE 17. (*a*) Sectionwise distributions of $C_{Dv'}$ (with values along the plate as well as in the two outer regions) and C_{Dp} (with values only along the plate); (*b*) sectionwise distributions of the volume vorticity lift components $C_{Dv}(\boldsymbol{\omega_x})$, $C_{Dv}(\boldsymbol{\omega_y})$ and $C_{Dv}(\boldsymbol{\omega_z})$ for the $AR = 1$ plate with $\alpha = 5°$, $Re = 300$ at $t = 0.72$.

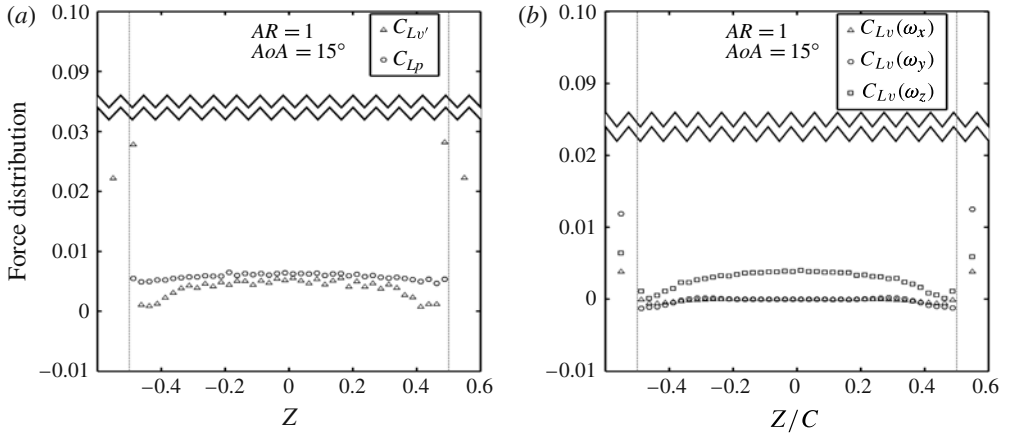

FIGURE 18. (*a*) Sectionwise distributions of $C_{Lv'}$ (with values along the plate as well as in the two outer regions) and C_{Lp} (with values only along the plate); (*b*) sectionwise distributions of the volume vorticity lift components $C_{Lv}(\boldsymbol{\omega_x})$, $C_{Lv}(\boldsymbol{\omega_y})$ and $C_{Lv}(\boldsymbol{\omega_z})$ for the $AR = 1$ plate with $\alpha = 15°$, $Re = 300$ at $t = 1.17$.

$\alpha = 15°$, we have in order $C_{Lv}(\boldsymbol{\omega_y})$ (=0.012), $C_{Lv}(\boldsymbol{\omega_z})$ (=0.006), $C_{Lv}(\boldsymbol{\omega_x})$ (=0.004). These values obviously indicate a stronger tip effect at the higher AoA $\alpha = 15°$. Next, we examine the corresponding force representations of C_{Dv} for the $AR = 1$ plate at $\alpha = 5$ and 15°, respectively. Figure 17(*b*) ($t = 0.72$, $\alpha = 5°$) shows that at this low AoA case all the three drag components $C_{Dv}(\boldsymbol{\omega_z})$, $C_{Dv}(\boldsymbol{\omega_x})$ and $C_{Dv}(\boldsymbol{\omega_y})$ have almost zero contributions. Figure 19(*b*) ($t = 1.17$, $\alpha = 15°$) shows that at this higher AoA case, the contribution of $C_{Dv}(\boldsymbol{\omega_z})$ is substantially over the entire span, where $C_{Dv}(\boldsymbol{\omega_x})$ and $C_{Dv}(\boldsymbol{\omega_y})$ still have little contributions. However, in the two outer regions all three drag components make significant contributions; and in the order of decreasing magnitude, we have $C_{Dv}(\boldsymbol{\omega_y}) = 0.004$, $C_{Dv}(\boldsymbol{\omega_z}) = 0.002$ and $C_{Dv}(\boldsymbol{\omega_x}) = 0.001$.

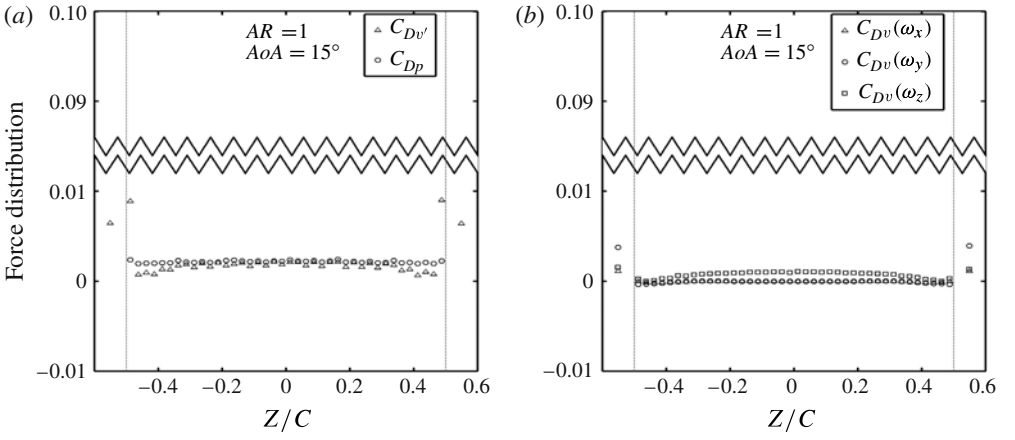

FIGURE 19. (*a*) Sectionwise distributions of $C_{Dv'}$ (with values along the plate as well as in the two outer regions) and C_{Dp} (with values only along the plate); (*b*) sectionwise distributions of the volume vorticity lift components $C_{Dv}(\boldsymbol{\omega_x})$, $C_{Dv}(\boldsymbol{\omega_y})$ and $C_{Dv}(\boldsymbol{\omega_z})$ for the $AR = 1$ plate with $\alpha = 15°$, $Re = 300$ at $t = 1.17$.

Next, we consider the lift for the case at the high AoA $\alpha = 45°$. Figures 13(*b*) and 15(*b*) show comparisons at two different flow stages ($t = 20$ and 1.56) for the $AR = 1$ plate at $\alpha = 45°$. At an early stage $t = 1.56$, the value in $C_{Lv}(\boldsymbol{\omega_z})$ is around 0.006 at the middle span, increasing slowly toward $|z| = 0.2$, but then declines quickly toward the two side edges. Although $C_{Lv}(\boldsymbol{\omega_x})$ and $C_{Lv}(\boldsymbol{\omega_y})$ are smaller than $C_{Lv}(\boldsymbol{\omega_z})$ distributed on the whole plate, they are still close to zero between $|z| < 0.1$, but vary unstably in the other regions of the plate due to LAR. In greater detail, $C_{Lv}(\boldsymbol{\omega_x})$ is almost zero in the midspan, becoming negative in the ranges of $0.2 < |z| < 0.45$, but turning to be positive further toward the two side edges. In contrast, $C_{Lv}(\boldsymbol{\omega_y})$ is also almost zero in the midspan, but behaves oppositely to $C_{Lv}(\boldsymbol{\omega_x})$ toward the two side edges. At the two outer regions, for both $C_{Lv}(\boldsymbol{\omega_x})$ and $C_{Lv}(\boldsymbol{\omega_y})$ we observe larger values compared with the low AoA cases; this reveals that the TiVs have strong effects on the force applied on the plate. The magnitude of the three components of C_{Lv} is $C_{Lv}(\boldsymbol{\omega_y})$, $C_{Lv}(\boldsymbol{\omega_x})$ and $C_{Lv}(\boldsymbol{\omega_z})$ in the decreasing order; and as a matter of fact $C_{Lv}(\boldsymbol{\omega_y})$ and $C_{Lv}(\boldsymbol{\omega_x})$ are 12 and 4 times the value of $C_{Lv}(\boldsymbol{\omega_z})$, respectively. We can also find out the influence range of tip effects based on distribution of $C_{Lv}(\boldsymbol{\omega_x})$ and $C_{Lv}(\boldsymbol{\omega_y})$. It is shown that both components vary noticeably in the ranges of $z < -0.3$ and $z > 0.3$; in other words, the influence range of tip effects is up to 60 % (=0.3/0.5). At the later stage $t = 20$ (figure 13*b*), the three contributions of C_{Lv} decline from their early values and become stable between $|z| < 0.4$. Only the values near the two side edges of the plate change significantly. At the two outer regions, the strengths of all three contributions of C_{Lv} weaken, compared with their values at the initial flow stage. In particular, $C_{Lv}(\boldsymbol{\omega_x})$ suffers a great decrease, becoming lower than the increased $C_{Lv}(\boldsymbol{\omega_z})$, while $C_{Lv}(\boldsymbol{\omega_y})$ remains the largest in magnitude. The influence range of tip effects is ∼20 % (=0.1/0.5). This indicates that the flow at the late time $t = 20$ exhibits better two-dimensionality than in the early stage $t = 1.56$. Next we consider the drag for the case at the high $\alpha = 45°$. The behaviours of their contributions are similar to those of C_{Lv} for both early and late time stages (see figures 20*b* and 21*b*). In other words, the contributions from $C_{Dv}(\boldsymbol{\omega_x})$ and $C_{Dv}(\boldsymbol{\omega_y})$ are significant, especially in the outer regions.

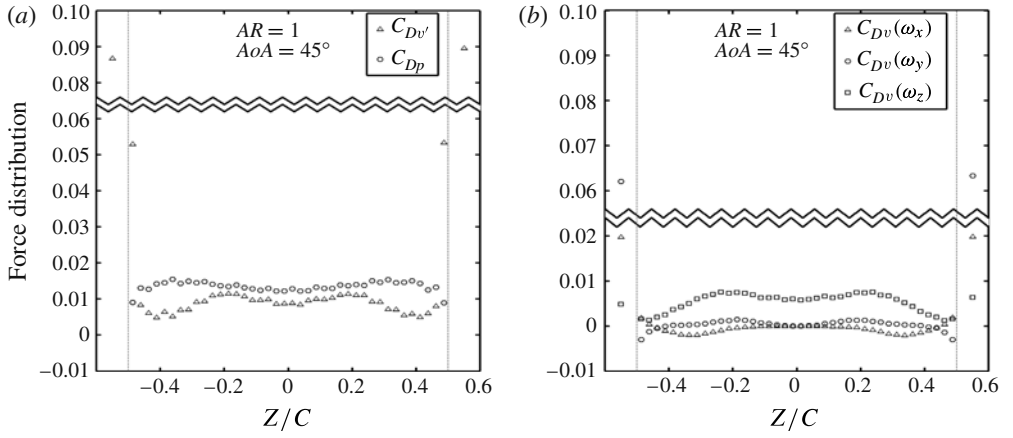

FIGURE 20. (*a*) Sectionwise distributions of $C_{Dv'}$ (with values along the plate as well as in the two outer regions) and C_{Dp} (with values only along the plate); (*b*) sectionwise distributions of the volume vorticity lift components $C_{Dv}(\boldsymbol{\omega_x})$, $C_{Dv}(\boldsymbol{\omega_y})$ and $C_{Dv}(\boldsymbol{\omega_z})$ for the $AR = 1$ plate with $\alpha = 45°$, $Re = 300$ at $t = 1.56$.

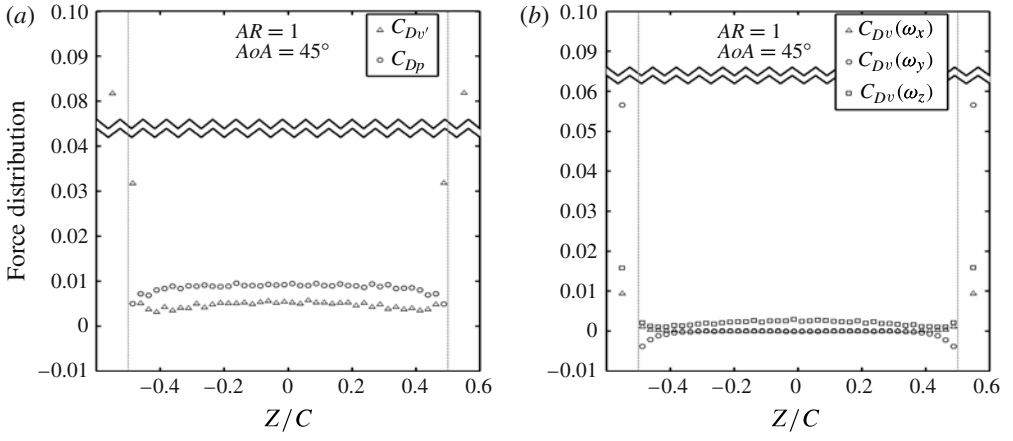

FIGURE 21. (*a*) Sectionwise distributions of $C_{Dv'}$ (with values along the plate as well as in the two outer regions) and C_{Dp} (with values only along the plate); (*b*) sectionwise distributions of the volume vorticity lift components $C_{Dv}(\boldsymbol{\omega_x})$, $C_{Dv}(\boldsymbol{\omega_y})$ and $C_{Dv}(\boldsymbol{\omega_z})$ for the $AR = 1$ plate with $\alpha = 45°$, $Re = 300$ at $t = 20.0$.

The difference in the force contributions between plates of aspect ratios 1 and 3 with the same AoA $\alpha = 45°$ is also of interest. Figure 15(*b*) shows the three components of C_{Lv} for the plate of $AR = 1$ at the early stage $t = 1.56$, while Figures 12(*b*) and 14(*b*) show the components for the $AR = 3$ plate at two flow stages: $t = 20$ and 0.46. The curve of $C_{Lv}(\boldsymbol{\omega_z})$ of $AR = 3$ at $t = 0.46$, which is arch-shaped, attains its maximum at the midspan, decreasing toward the two side edges. In the meanwhile, $C_{Lv}(\boldsymbol{\omega_x})$ and $C_{Lv}(\boldsymbol{\omega_y})$ make almost no contribution to the force, except those in the ranges between $|z| = 1.30$ and 1.50. At the outer regions, there is obvious a tip effect that in the order of decreasing magnitude we have $C_{Lv}(\boldsymbol{\omega_y}) = 0.043$, $C_{Lv}(\boldsymbol{\omega_z}) = 0.018$ and $C_{Lv}(\boldsymbol{\omega_x}) = 0.003$.

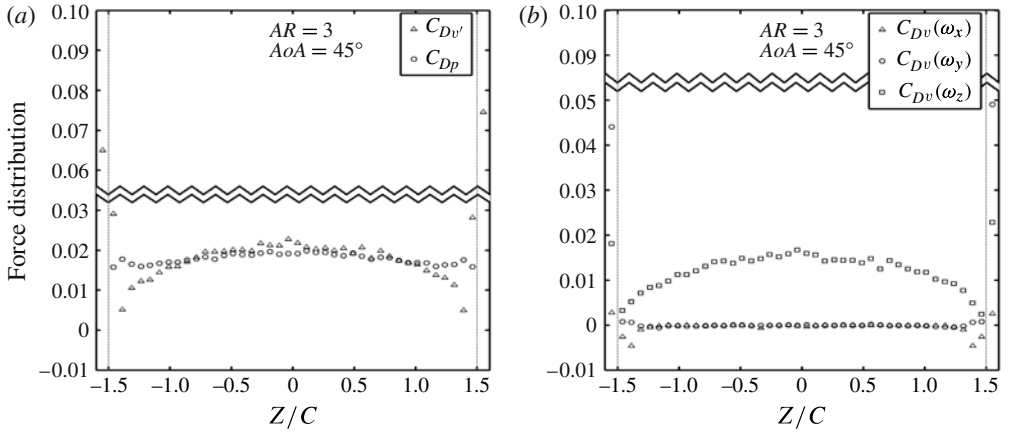

FIGURE 22. (*a*) Sectionwise distributions of $C_{Dv'}$ (with values along the plate as well as in the two outer regions) and C_{Dp} (with values only along the plate); (*b*) sectionwise distributions of the volume vorticity lift components $C_{Dv}(\boldsymbol{\omega_x})$, $C_{Dv}(\boldsymbol{\omega_y})$ and $C_{Dv}(\boldsymbol{\omega_z})$ for the $AR = 3$ plate with $\alpha = 45°$, $Re = 300$ at $t = 0.46$.

AoA	Aspect ratio	Early time	Late time
5	1	$C_{Lv}(\boldsymbol{\omega_z}) > C_{Lv}(\boldsymbol{\omega_y}) > C_{Lv}(\boldsymbol{\omega_x})$	$C_{Lv}(\boldsymbol{\omega_y}) > C_{Lv}(\boldsymbol{\omega_z}) > C_{Lv}(\boldsymbol{\omega_x})$
5	1	$C_{Dv}(\boldsymbol{\omega_z}) \sim C_{Dv}(\boldsymbol{\omega_y}) \sim C_{Dv}(\boldsymbol{\omega_x})$	$C_{Dv}(\boldsymbol{\omega_y}) > C_{Dv}(\boldsymbol{\omega_z}) > C_{Dv}(\boldsymbol{\omega_x})$
15	1	$C_{Lv}(\boldsymbol{\omega_y}) > C_{Lv}(\boldsymbol{\omega_z}) > C_{Lv}(\boldsymbol{\omega_x})$	$C_{Lv}(\boldsymbol{\omega_y}) > C_{Lv}(\boldsymbol{\omega_z}) > C_{Lv}(\boldsymbol{\omega_x})$
15	1	$C_{Dv}(\boldsymbol{\omega_y}) > C_{Dv}(\boldsymbol{\omega_z}) > C_{Dv}(\boldsymbol{\omega_x})$	$C_{Dv}(\boldsymbol{\omega_y}) > C_{Dv}(\boldsymbol{\omega_z}) > C_{Dv}(\boldsymbol{\omega_x})$
45	1	$C_{Lv}(\boldsymbol{\omega_y}) > C_{Lv}(\boldsymbol{\omega_x}) > C_{Lv}(\boldsymbol{\omega_z})$	$C_{Lv}(\boldsymbol{\omega_y}) > C_{Lv}(\boldsymbol{\omega_z}) > C_{Lv}(\boldsymbol{\omega_x})$
45	1	$C_{Dv}(\boldsymbol{\omega_y}) > C_{Dv}(\boldsymbol{\omega_x}) > C_{Dv}(\boldsymbol{\omega_z})$	$C_{Dv}(\boldsymbol{\omega_y}) > C_{Dv}(\boldsymbol{\omega_z}) > C_{Dv}(\boldsymbol{\omega_x})$
45	3	$C_{Lv}(\boldsymbol{\omega_y}) > C_{Lv}(\boldsymbol{\omega_z}) > C_{Lv}(\boldsymbol{\omega_x})$	$C_{Lv}(\boldsymbol{\omega_y}) > C_{Lv}(\boldsymbol{\omega_z}) > C_{Lv}(\boldsymbol{\omega_x})$
45	3	$C_{Dv}(\boldsymbol{\omega_y}) > C_{Dv}(\boldsymbol{\omega_z}) > C_{Dv}(\boldsymbol{\omega_x})$	$C_{Dv}(\boldsymbol{\omega_y}) > C_{Dv}(\boldsymbol{\omega_z}) > C_{Dv}(\boldsymbol{\omega_x})$

TABLE 1. Relation of individual force contributions in the outer regions.

In contrast, the curve of $C_{Lv}(\boldsymbol{\omega_z})$ of $AR = 1$ at $t = 1.56$ is in a double-hump shape, with the saddle in the midspan, decreasing toward the two side edges. In the meanwhile, $C_{Lv}(\boldsymbol{\omega_x})$ and $C_{Lv}(\boldsymbol{\omega_y})$ have much smaller contribution, except the part in the ranges between $|z| = 1.30$ and 1.50. At the outer regions, a stronger tip effect is observed that both of $C_{Lv}(\boldsymbol{\omega_x})$ and $C_{Lv}(\boldsymbol{\omega_y})$ are larger than $C_{Lv}(\boldsymbol{\omega_z})$, and in the decreasing order of magnitude we have $C_{Lv}(\boldsymbol{\omega_y}) = 0.06$, $C_{Lv}(\boldsymbol{\omega_x}) = 0.02$ and $C_{Lv}(\boldsymbol{\omega_z}) = 0.005$. Now consider the plate of $AR = 3$ when the flow evolves to the large time $t = 20$ (figure 12*b*). The component $C_{Lv}(\boldsymbol{\omega_z})$ obviously declines, and $C_{Lv}(\boldsymbol{\omega_x})$ and $C_{Lv}(\boldsymbol{\omega_y})$ have almost no contributions except in the regions near the two side edges. At the two outer regions, the vorticity lift forces $C_{Lv}(\boldsymbol{\omega_y})$ and $C_{Lv}(\boldsymbol{\omega_z})$ weaken in strength, while $C_{Lv}(\boldsymbol{\omega_x})$ gains a little, and in the order of decreasing magnitude we have $C_{Lv}(\boldsymbol{\omega_y}) = 0.024$, $C_{Lv}(\boldsymbol{\omega_z}) = 0.005$ and $C_{Lv}(\boldsymbol{\omega_x}) = 0.004$.

Next, we consider C_{Dv} for the $AR = 3$ plate at the early $t = 0.46$ (figure 22*b*) and the later $t = 20$ (figure 23*b*). Note that all behaviours of the three components of C_{Dv} are the same as those of C_{Lv} at two flow stages: $C_{Dv}(\boldsymbol{\omega_z})$ along the plate span is a source of large drag, and $C_{Dv}(\boldsymbol{\omega_y})$ is responsible for generation of some drag force

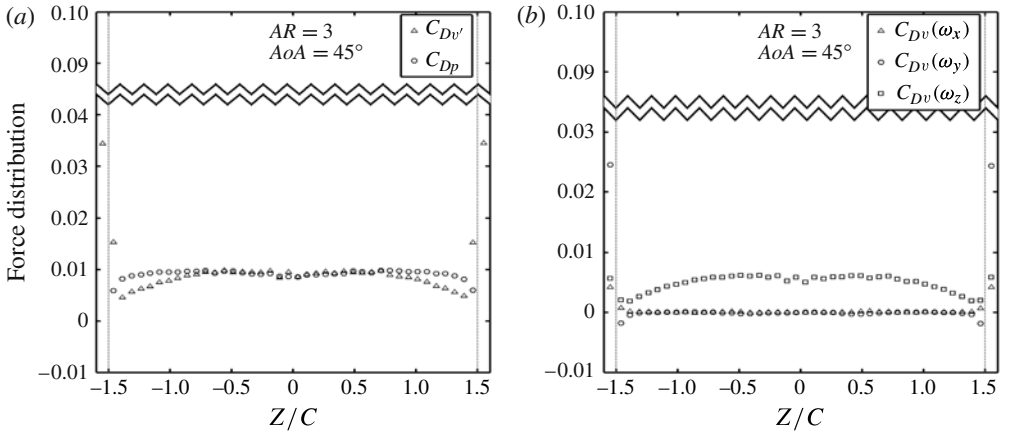

FIGURE 23. (*a*) Sectionwise distributions of $C_{Dv'}$ (with values along the plate as well as in the two outer regions) and C_{Dp} (with values only along the plate); (*b*) sectionwise distributions of the volume vorticity lift components $C_{Dv}(\boldsymbol{\omega_x})$, $C_{Dv}(\boldsymbol{\omega_y})$ and $C_{Dv}(\boldsymbol{\omega_z})$ for the $AR = 3$ plate with $\alpha = 45°$, $Re = 300$ at $t = 20.0$.

(see $AR = 3$, $\alpha = 45°$, $t = 0.46$ figure 22*b* and $AR = 3$, $\alpha = 45°$, $t = 20$ figure 23*b*). It is of interest to summarize the relative importance of individual force contributions in the outer regions. Table 1 lists the results. At late times, for both lift and drag the order of significance is definite: we have the $C_{Lv}(\boldsymbol{\omega_y}) > C_{Lv}(\boldsymbol{\omega_z}) > C_{Lv}(\boldsymbol{\omega_x})$ ($C_{Dv}(\boldsymbol{\omega_y}) > C_{Dv}(\boldsymbol{\omega_z}) > C_{Dv}(\boldsymbol{\omega_x})$). In other words, the TiVs contribute to the forces largely through the *y*-component, yet less through the *x*-component. At early times, the situations are more complicated. When the AoA is small ($\alpha = 5°$), the *z*-component is the major contribution because the TiVs are quite weak. As the AoA is increased to 15°, the *y*-component exceeds the *z*-component, becoming the largest contribution. At the even large angle 45° the *y*-component remains the largest, however, we see a distinction in the *x*- and *z*-components between the lower and larger aspect ratio plates. For the LAR plate ($AR = 1$), we have $C_{Lv}(\boldsymbol{\omega_x}) > C_{Lv}(\boldsymbol{\omega_z})$ ($C_{Dv}(\boldsymbol{\omega_x}) > C_{Dv}(\boldsymbol{\omega_z})$), while for the larger aspect ratio plate ($AR = 3$), we have $C_{Lv}(\boldsymbol{\omega_z}) > C_{Lv}(\boldsymbol{\omega_x})$ ($C_{Dv}(\boldsymbol{\omega_z}) > C_{Dv}(\boldsymbol{\omega_x})$). This indicates that for lower $AR = 1$ plate, the TiVs are so strong at the early stage, both transverse components (*y* and *x*) could be larger than the longitudinal *z*-component in magnitude.

On the other hand, $C_{Lv}(\boldsymbol{\omega_z})$ and $C_{Dv}(\boldsymbol{\omega_z})$ constitute the major contributions to the lift and drag along the plate span, respectively. Along the plate span $C_{Lv}(\boldsymbol{\omega_z})$ and $C_{Dv}(\boldsymbol{\omega_z})$ are always able to provide, respectively, positive lift and drag to the plate for all of the cases under investigation, especially for a plate of larger aspect ratio at large AoA (>20°). Nevertheless, the actual contribution to the forces is the resultant of mutual interactions between the vortices over the plate and the TiVs. The influence range of the TiVs for the $AR = 1$ plate could be up 60 % of the span width in the early flow stage, while for $AR = 3$ it is only ∼10 %. Finally it is also noted that as time evolves all of the components of C_{Lv} and C_{Dv}, including the parts over the plate and those in the outer regions, decrease in strengths with the LEVs, TEVs and TiVs extending downstream and their vorticity being diffused.

It is also interesting to investigate the three-dimensional effects by calculating the relative force contributions due to the transverse vorticity components (ω_x and ω_y). Tables 2 and 3 show, respectively, the ratios of $C_{Lv}(\boldsymbol{\omega_x}, \boldsymbol{\omega_y})/C_{Lv}$ and $C_{Dv}(\boldsymbol{\omega_x}, \boldsymbol{\omega_y})/C_{Dv}$

AR	α (deg.)	$t=1$	$t=2$	$t=3$	$t=5$	$t=10$	$t=15$
1	5	10.9	23.8	27.2	32.1	27.7	28.2
	10	10.7	21.4	24.5	29.8	30.1	30.4
	15	11.6	22.4	26.5	29.2	30.6	30.6
	30	21.8	32.1	37.2	42.1	45.7	46.9
	45	31.8	41.6	45.3	46.8	48.9	50.0
	60	39.4	43.9	47.8	50.1	49.7	49.4
2	5	0.8	7.1	9.3	9.7	10.6	11.0
	10	1.5	6.6	9.6	9.6	10.9	11.7
	15	4.8	8.7	11.8	14.3	16.2	16.6
	30	10.0	17.4	23.6	26.4	28.7	29.2
	45	16.2	27.3	30.7	30.6	31.6	31.6
	60	22.0	31.4	33.6	32.6	30.3	30.6
3	5	0.2	3.5	4.5	5.5	5.2	6.8
	10	1.3	4.3	5.4	6.5	7.2	7.1
	15	2.5	5.2	7.0	9.4	10.6	10.9
	30	5.6	11.1	19.5	14.5	19.3	20.2
	45	9.8	17.9	24.1	21.0	21.7	21.3
	60	13.7	22.3	26.8	23.4	21.8	22.5

TABLE 2. Ratios of the x- and y-direction vorticity lift coefficients to the total lift coefficients ($C_{Lv}(\boldsymbol{\omega_x}, \boldsymbol{\omega_y})/C_{Lv}$) (%) versus $AR = 1$, 2 and 3 plates at six different AoAs α.

AR	α (deg.)	$t=1$	$t=2$	$t=3$	$t=5$	$t=10$	$t=15$
1	5	16.4	34.8	40.6	46.5	43.6	43.7
	10	13.5	24.7	28.7	33.8	34.4	34.8
	15	14.5	26.2	30.4	33.4	34.9	34.9
	30	24.0	34.4	39.4	44.2	47.6	48.7
	45	34.6	44.2	47.5	48.8	50.5	51.7
	60	43.1	47.1	49.9	52.1	51.7	51.3
2	5	1.2	11.8	15.6	16.5	19.0	19.8
	10	2.0	8.7	12.1	13.0	14.6	15.6
	15	5.3	9.8	13.3	16.1	18.4	18.8
	30	11.1	18.6	24.8	27.6	29.8	30.2
	45	17.6	29.0	31.9	31.8	32.8	32.9
	60	23.9	33.5	34.5	33.7	31.4	31.9
3	5	0.1	6.8	8.8	10.3	10.5	11.8
	10	1.3	5.0	6.7	8.1	9.3	9.4
	15	2.8	6.0	7.9	10.4	12.0	12.4
	30	6.1	11.7	20.0	15.4	20.1	21.1
	45	10.5	18.8	24.9	21.8	22.1	22.3
	60	14.8	23.7	27.5	24.4	22.6	23.5

TABLE 3. Ratios of the x- and y-direction vorticity drag coefficients to the total drag coefficients ($C_{Dv}(\boldsymbol{\omega_x}, \boldsymbol{\omega_y})/C_{Dv}$) (%) versus $AR = 1$, 2 and 3 plates at six different AoAs α.

at six different time instants, from which we observed that they form diverse fractions for different aspect ratios as well as low and high AoAs. First of all, given the same aspect ratio plate the ratio $C_{Lv}(\boldsymbol{\omega_x}, \boldsymbol{\omega_y})/C_{Lv}$ basically becomes larger at all times with increasing the AoA. In all of the cases under consideration, the $C_{Lv}(\boldsymbol{\omega_x}, \boldsymbol{\omega_y})/C_{Lv}$ tends to be stationary at later times (say, $t = 15$). The ratio $C_{Lv}(\boldsymbol{\omega_x}, \boldsymbol{\omega_y})/C_{Lv}$ is larger when

Ratios (outer regions)	AR	Early (%)	Late (%)
C_{Lv}(outer)/C_{Lv}(total)	1	33.44	50.37
	3	17.64	19.23
C_{Dv}(outer)/C_{Dv}(total)	1	35.52	51.73
	3	19.21	19.42
$C_{Lv}(\boldsymbol{\omega_x}, \boldsymbol{\omega_y})$(outer)/$C_{Lv}$(outer)	1	93.67	80.53
	3	70.69	87.34
$C_{Dv}(\boldsymbol{\omega_x}, \boldsymbol{\omega_y})$(outer)/$C_{Dv}$(outer)	1	93.61	80.62
	3	70.64	84.74

TABLE 4. Ratios of force contributions in the two outer regions at early and late-time stages for the plates of $AR = 1$ and 3 at $\alpha = 45°$ with $Re = 300$.

we have a shorter plate at higher AoA. The ratio $C_{Lv}(\boldsymbol{\omega_x}, \boldsymbol{\omega_y})/C_{Lv}$ increases with the decrease in aspect ratio for the obvious reason that there is an decrease in the contribution due to $\boldsymbol{\omega_z}$-vorticity, including LEVs and TEVs. For instance, the plate with $AR = 2$ at $\alpha = 45°$ has $C_{Lv}(\boldsymbol{\omega_x}, \boldsymbol{\omega_y})/C_{Lv} = 16.2\,\%$ at $t = 1$, and $31.6\,\%$ at $t = 15$. In contrast, the plate with $AR = 3$ at $\alpha = 10°$ has $C_{Lv}(\boldsymbol{\omega_x},\boldsymbol{\omega_y})/C_{Lv} = 1.3\,\%$ at $t = 1$, and $7.1\,\%$ at $t = 15$. Notably for the plate with $AR = 1$, the contribution from $\boldsymbol{\omega_x}$- and $\boldsymbol{\omega_y}$-direction vorticity at high AoA can initially attain up to 20–40 %, and can even make nearly one half of C_{Lv} with increase in time. This is because as the intertwined vortex structure (LEVs, TEVs, TiVs) extends downstream, its strength is decreasing, in particular the z-direction vorticity associated with the LEV is weaken significantly. As an example, the plate with $AR = 1$ plate at $\alpha = 45°$ has $C_{Lv}(\boldsymbol{\omega_x}, \boldsymbol{\omega_y})/C_{Lv} = 31.8\,\%$ at $t = 1$ and $50.0\,\%$ at $t = 15$.

Next, we examine the same analysis for the drag coefficients. Table 3 shows that the variation in trends and ratios for the drag is approximately comparable to the lift. One distinguished point is noted for the short plate with $AR = 1$ at $\alpha = 5°$. The ratio $C_{Dv}(\boldsymbol{\omega_x}, \boldsymbol{\omega_y})/C_{Dv}$ is at all times larger than its values for the same plate at the higher AoA $\alpha = 10°$ (and even 15°). This trend becomes weaker and occurs later in time for the plate with a larger aspect ratio (=2, 3). It is also noted that C_{Dv} increase with increasing the AoA. This indicates that at the low AoA $\alpha = 5°$, the contribution from the longitudinal component to the drag is not so significant as it is at higher AoA. As we increase the AoA in the range of $\alpha > 10°$, the contributions from both of the transverse $(\boldsymbol{\omega_x}, \boldsymbol{\omega_y})$ and longitudinal $\boldsymbol{\omega_z}$ are also increased, but the increase in the transverse components is more significant. As a result, the ratio $C_{Dv}(\boldsymbol{\omega_x}, \boldsymbol{\omega_y})/C_{Dv}$ increases with increasing the AoA.

It is of interest by the VFA to see how much of the lift or drag is contributed by the vortices in the outer region. Also of interest is the importance of the relative contributions from the transverse components to the longitudinal component. Table 4 shows the lift and drag ratios for the plates with $AR = 1$ and 3 at $\alpha = 45°$ at early and late time stages with the same $Re = 300$. The effect from the outer region is more notable at $AR = 1$ than at $AR = 3$ from the numerical evidence. The ratio C_{Lv}(outer)/C_{Lv}(total) = 33.44 % for $AR = 1$ is 1.8 times that of $AR = 3$ in the early stage, while the ratio C_{Lv}(outer)/C_{Lv}(total) = 50.37 % for $AR = 1$ is even 2.6 times that of $AR = 3$ at the later time stage. The plate with $AR = 3$, the ratio C_{Lv}(outer)/C_{Lv}(total) remains unchanged in time, indicating that the effect from the outer region for the longer plate is soon developed and then varies little as a whole, although the details do change as time evolves. Moreover, the ratio $C_{Lv}(\boldsymbol{\omega_x}, \boldsymbol{\omega_y})/C_{Lv}$

in the outer region further reveals the opposite trends for $AR = 1$ and $AR = 3$. Its value decreases from the early stage to the later time stage for the short plate with $AR = 1$, but increases for the longer plate with $AR = 3$. This illustrates the following fact. Relatively speaking, the effect of producing lift by generating $\boldsymbol{\omega}_x$ and $\boldsymbol{\omega}_y$ in the outer regions for the short plate is more significant right after the impulsive start, yet the effect of the lift-generating mechanism in the outer regions for the longer plate is still under development after the start. It is reasonable though not precisely to consider that $\boldsymbol{\omega}_z$ is mainly contributed by the LEV, while $\boldsymbol{\omega}_x$ and $\boldsymbol{\omega}_y$ are contributed by the TiVs. The above results show that (i) for the shorter plate ($AR = 1$), the LEV is suppressed by the TiVs in the initial stage, and then develops gradually, extending its vorticity beyond the outer edges; while on the other hand, (ii) for the longer plate ($AR = 3$), the TiVs are initially suppressed by the strong LEV, but have more room for development in later stages as the LEV weakens in strength because of diffusion.

5. Concluding remarks

The vorticity forces on an impulsively started finite plate have been analysed with a force element representation. In particular, we made comparisons between the VFA and the PFA by examining the effects of the aspect ratio ($AR = 1$, 2 or 3) and of the AoA (5, 10, 15, 30, 45 and 60°). The Reynolds number Re is either 100 or 300.

The force element analysis provides a means for identifying the regions of vorticity responsible for force contributions. The summary is focused on the lift as the behaviours in the drag are similar. It is shown that there are four regions of distinguishable vortex structures. Above all, it is noted that the LEV has a separation bubble in the x–y plane for sections near the midspan, and is connected to the TiVs, the side edges where the roll-up structure contains a separation bubble above the plate in the y–z plane. First, the LEV contributes large positive lift elements, yet in sections near the midspan, there are negative elements inside the separation bubble. Second, the part of each TiV above the extended plate contributes large positive lift elements, while along the downstream direction, there is a developing region of negative elements inside each separation bubble. Third, we have strong positive elements in the two regions where the LEV and TiVs interlink and rotate against each other. Each of the regions grows and moves inward toward the midspan as the flow is developed downstream. Fourth, the velocity field in the slender region just below the plate contributes substantially negative lift elements. The LEV, TiVs and TEV are interwoven to form a complete vorticity-loop structure. As long as the loop structure is extending downstream of the finite wing, its contribution to the lift is quickly diminished.

The force element approach is different from the classical aerodynamic theory. The latter considers the downwash flow of the TiVs as the cause of reduction in the lift of a finite wing as compared with its two-dimensional counterpart. The former, on the other hand, considers that, as there is no longer a genuinely two-dimensional flow for a finite wing, it is more meaningful to examine directly the contribution from the TiVs to the lift. Indeed, the force element theory shows that the TiVs are strong sources of lift. In other words, TiVs and LEV as sources of lift (and other force components) are considered on an equal basis; TiVs generated by the side edges, like the LEV generated by the front edges, work collaboratively with the LEV in contributing lift. Although LEVs, TiVs as well as TEVs are useful concepts to describe a vortex (a lump of fluid), they are difficult to define without ambiguities as there are no clear boundaries among them. Instead, the force element theory enables us to examine the

force contributions from any subset of the flow region with non-zero vorticity. To summarize, we describe the features for the lift analysis; the analysis for the drag is similar.

In the flow past a finite plate, not only is there spanwise (longitudinal) vorticity, but are also there vorticity components in the other two orthogonal (transverse) directions. In order to examine the three-dimensional effects, we provided two viewpoints: (i) SVF distribution ($C_{Dv'}$, $C_{Lv'}$) contrasted with the traditional pressure force distribution (C_{Lp}, C_{Dp}), and (ii) the force credited to orthogonal (transverse) components (ω_x, ω_y, ω_z) contrasted with all of the total force (C_D, C_L) credited to all of the vorticity components in the entire flow region as well as in the outer regions. It is noted that in the ideal case of two-dimensional flow, there are no outer regions, and $C_{Lv'}$ and C_{Lp} are identical, and $C_{Dv'}$ and C_{Dp} are identical. Both viewpoints based on the force element theory show distinguished differences at different aspect ratios and AoAs, and between the early and later stages of flow development.

Consider the lift force from viewpoint 1. At the lower aspect ratio $AR = 1$, the SPF is always larger than the SVF in the plate region. The deficit of SVF as compared with SPF in the plate region is made up of the positive SVF contribution in the outer regions. The difference between SPF and SVF is more conspicuous at large α. At the large $AR = 3$, the SPF and SVF are usually small in the middle plate region; the discrepancy occurs near the outer edges of the plate. However, the situation changes in the case of a large AoA (say, $\alpha = 45°$). In the initial transient, SVF may exceed SPF in the middle of the plate, and becomes much smaller towards the edges of the plate. In the nearly steady state, the difference is small in the middle region of the plate, and becomes large farther from this region.

Consider the lift force from viewpoint 2. In the early stages just after the flow is started, the force component due to ω_z dominates other components in the plate region. But the other force components due to ω_x and ω_y have also been developed in the outer region and may exceed the component of ω_z in magnitude. Then, in all of the cases under consideration, it is found that all of the lift components due respectively to ω_x, ω_y and ω_z in the outer regions are positive, and the lift component due to ω_y is invariably the largest at the later time. At the larger aspect ratio $AR = 3$, the lift components due to ω_x and ω_y are typically small in the middle plate region, but may exhibit negative contributions at the outer edges of the plate region. At a lower aspect ratio $AR = 1$ but a larger α, the lift components due to ω_x and ω_y may become substantial in the plate region, although still small compared with that due to ω_z. It is reasonable to consider that ω_z is mainly contributed by the LEV, while ω_x and ω_y are contributed by the TiVs. The present analysis shows that temporal variations of the relative importance of force contributions strongly depend on the interplay between the two vortex systems. (i) For the shorter plate ($AR = 1$), the LEV is suppressed by the TiVs in the initial stage, and then develops gradually, extending its vorticity beyond the outer edges. (ii) For the longer plate ($AR = 3$), the TiVs are initially suppressed by the strong LEV, but have more room for development in later stages as the LEV weakens in strength because of diffusion.

The sectionwise force analysis along the wing span by both SVF (VFA) and SPF (PFA) facilitates identification of three-dimensional signatures of flow past a truncated finite wing. Moreover, the VFA based on the force element representation for assessing the relative importance of individual vorticity components and of contributions from different regions can be pursued for all kinds of finite wings by relating the flow features directly to the aerodynamics forces that have no two-dimensional counterparts, such as those of a delta wing and of many natural flights.

Acknowledgements

The work was supported in part by the National Science Council of the Republic of China (Taiwan) under the Contract No. NSC97-2221-E-002-223-MY3 (C. C. Chang) and No. 98-2221-E-002-094-MY3 (C. C. Chu).

REFERENCES

BARTLETT, G. E. & VIDAL, R. J. R. 1955 Experimental investigation of influence of edge shape on the aerodynamic characteristics of low aspect ratio wings at low speeds. *J. Aero. Sci.* **22**, 517–533.

BIESHEUVEL, A. & HAGMEIJER, R. 2006 On the force on a body moving in fluid. *Fluid Dyn. Res.* **38**, 716–742.

BIRCH, J. M., DICKSON, W. B. & DICKINSON, M. H. 2004 Force production and flow structure of the leading edge vortex on flapping wings at high and low Reynolds numbers. *J. Expl. Biol.* **207**, 1063–1072.

BOLLAY, W. 1939 A nonlinear wing theory and its application to rectangular wings of small aspect ratio. *Z. Angew. Math. Mech.* **19**, 21–35.

BURGERS, J. M. 1920 On the resistance of fluids and vortex motion. *Proc. Kon. Akad. Westenschappente Amsterdam* **1**, 774–782.

CHANG, C. C. 1992 Potential flow and forces for incompressible viscous flow. *Proc. R. Soc. A-Math. Phys. Eng. Sci.* **437**, 517–525.

CHANG, C. C., YANG, S. H. & CHU, C. C. 2008 A many-body force decomposition with applications to flow about bluff bodies. *J. Fluid Mech.* **600**, 95–104.

COSYN, P. & VIERENDEELS, J. 2006 Numerical investigation of low-aspect-ratio wings at low Reynolds numbers. *J. Aircraft* **43**, 713–722.

ELLINGTON, C. P., VAN DEN BERG, C., WILLMOTT, A. P. & THOMAS, A. L. R. 1996 Leading-edge vortices in insect flight. *Nature* **384**, 626–630.

FREYMUTH, P., BANK, W. & FINAISH, F. 1987 Further visualization of combined wing tip and starting vortex systems. *AIAA J.* **25**, 1153–1159.

HOWARTH, L. 1935 The theoretical determination of the lift coefficient for a thin elliptic cylinder. *Proc. R. Soc. Lond. Ser.* A **149**, 558–586.

HOWE, M. S. 1995 On the force and moment on a body in an incompressible fluid, with application to rigid bodies and bubbles at high and low Reynolds numbers. *Quart. J. Mech. Appl. Math.* **48**, 401–426.

HOWE, M. S., LAUCHLE, G. C. & WANG, J. 2001 Aerodynamic lift and drag fluctuations of a sphere. *J. Fluid Mech.* **436**, 41–57.

HSIEH, C. T., CHANG, C. C. & CHU, C. C. 2009 Revisiting the aerodynamics of hovering flight using simple models. *J. Fluid Mech.* **623**, 121–148.

HSIEH, C. T., KUNG, C. F., CHANG, C. C. & CHU, C. C. 2010 Unsteady aerodynamics of dragonfly using a simple wing-wing model from the perspective of a force decomposition. *J. Fluid Mech.* **663**, 233–252.

HUNT, J. C. R., WRAY, A. A. & MOIN, P. 1988 Eddies, stream, and convergence zones in turbulent flows, *Center for Turbulence Research Report CTR-S88*, pp. 193–208.

KAMBE, T. 1986 Acoustic emissions by vortex motions. *J. Fluid Mech.* **173**, 643–666.

KIM, D & GHARIB, M. 2010 Experimental study of three-dimensional vortex structures in translating and rotating plates. *Exp. Fluids.* **49**, 329–339.

LAMAR, J. E. 1974 Extension of leading-edge-suction analogy to wings with separated flow around the side edges at subsonic speeds. NASA TR R-428, L-9460.

LAMAR, J. E. 1976 Prediction of vortex flow characteristics of wings at subsonic and supersonic speeds. *J. Aircraft* **13**, 490–494.

LANDAU, L. D. & LIFSHITZ, E. M. 1987 *Fluid Mechanics*, 2nd edn. Pergamon.

LIGHTHILL, M. J. 1979 Wave and hydrodynamic loading. *Proc. Second Intl Conf. Behaviour Off-Shore Struct., BHRA Cranfield* **1**, 1–40.

LIGHTHILL, M. J. 1986 Fundamentals concerning wave loading on offshore structures. *J. Fluid Mech.* **173**, 667–681.

MAGNAUDET, J. 2011 A 'reciprocal' theorem for the prediction of loads on a body moving in an inhomogeneous flow at arbitrary Reynolds number. *J. Fluid Mech.* **689**, 564–604.

MAXWORTHY, T. 1979 Experiments on the Weis-Fogh mechanism of lift generation by insects in hovering flight. Part I. Dynamics of the fling. *J. Fluid Mech.* **93**, 47–63.

PAYNE, R. B. 1958 Calculations of unsteady flow past a circular cylinder. *J. Fluid Mech.* **3**, 81–86.

PHILLIPS, O. M. 1956 The intensity of aeolian tones. *J. Fluid Mech.* **1**, 607–624.

POLHAMUS, E. C. 1971 Predictions of vortex-lift characteristics by a Leading–Edge–Suction analogy. *J. Aircraft* **8**, 193–199.

QUARTAPELLE, L. & NAPOLITANO, M. 1983 Force and moment in incompressible flows. *AIAA J.* **22**, 1713–1718.

RINGUETTE, M. J., MILANO, M. & GHARIB, M. 2007 Role of the tip vortex in the force generation of low-aspect-ratio normal flat plates. *J. Fluid Mech.* **581**, 453–468.

SEARS, W. R. 1956 Some recent developments in airfoil theory. *J. Aeronaut. Sci.* **23**, 490–499.

SEARS, W. R. 1976 Unsteady motion of airfoil with boundary layer separation. *AIAA J.* **14**, 216–220.

SHYY, W., AONO, H., CHIMAKURTHI, S. K., TRIZILA, P., KANG, C. K., CESNIK, C. E. S. & LIU, H. 2010 Recent progress in flapping wing aerodynamics and aeroelasticity. *Prog. Aeronaut. Sci.* **46**, 254–327.

TAIRA, K. & COLONIUS, T. 2009 Three-dimensional separated flows around low-aspect-ratio flat plates. *J. Fluid Mech.* **623**, 187–207.

TORRES, G. E. & MUELLER, T. J. 2004 Low-aspect-ratio wing aerodynamics at low Reynolds numbers. *AIAA J.* **42** (5), 865–873.

WELLS, J. C. 1996 A geometrical interpretation of force on a translating body in rotational flow. *Phys. Fluids* **8**, 442–450.

WINTER, H. 1936 Flow phenomena on plates and aerofoils of short span. *Tech. Rep.* TM 798, NACA.

WU, J. C. 1981 Theory for aerodynamic force and moment in viscous flows. *AIAA J.* **19**, 432–441.